Available online at www.sciencedirect.com
ScienceDirect
Comput. Methods Appl. Mech. Engrg. 410 (2023) 116040
Computer methods in applied mechanics and engineering
www.elsevier.com/locate/cma

A novel BEM-DEM coupling in the time domain for simulating dynamic problems in continuous and discontinuous media

Guilherme Barros[a,*], Victor Sapucaia[c], Philipp Hartmann[a], Andre Pereira[c], Jerzy Rojek[b], Klaus Thoeni[a]

[a] Centre for Geotechnical Science and Engineering, The University of Newcastle, 2308 Callaghan, Australia
[b] Institute of Fundamental Technological Research, Polish Academy of Sciences, Pawinskiego 5B, 02-106 Warsaw, Poland
[c] Institute of Computing, Fluminense Federal University, Rua Passo da Patria 156, Niterói 24210-240, Brazil

Received 16 February 2023; received in revised form 28 March 2023; accepted 29 March 2023
Available online xxxx

Abstract

This work presents a novel scheme to couple the Boundary Element Method (BEM) and the Discrete Element Method (DEM) in the time domain. The DEM captures discontinuous material behaviour, such as fractured and granular media. However, applying the method to real-life applications embedded into infinite domains is challenging. The authors propose a solution to this challenge by coupling the DEM with the BEM. The capability of the BEM to model infinite domains accurately and efficiently, without the need for numerical artifices, makes it the perfect complement to the DEM. This study proposes a direct monolithic interface-based coupling method that resolves any incompatibilities between the two methods in two dimensions. The benchmark results show that the proposed methodology consistently produces results that align with analytical solutions. The final example in the paper showcases the full potential of this innovative methodology, where the DEM models a fracturing process, and the BEM evaluates its far-field effect.

Keywords: Discrete Element Method (DEM); Boundary Element Method (BEM); Discontinuous materials; Wave propagation; Infinite domain; Monolithic coupling

1. Introduction

Engineers often resort to numerical simulation to study dynamic problems such as blasting processes [1–3], earthquakes [4,5], ballistic impacts [6] among others. Blasting has several applications, such as tunnelling [7] and mining [8]. Dynamic simulations are also valuable for the simulation of excavations [9,10] and rock cutting [11]. Numerical models used in such simulations need to be capable of capturing discontinuous material behaviours, such as fracturing and fragmentation in rocks and granular movement in the soil [12], and at the same time, have to represent properly shock-induced wave propagation and, in some cases, soil–structure interaction [13].

Different numerical methods are used for dynamic simulations, the Finite Element Method (FEM) being the most popular one [3,6,14]. The Finite Difference Method (FDM) is another numerical method which can be applied to

* Corresponding author.
E-mail address: guilherme.coelhogomesbarros@uon.edu.au (G. Barros).

https://doi.org/10.1016/j.cma.2023.116040

simulate seismic waves [15,16]. Both the FEM and FDM can only handle finite domains, while real-life applications are often within infinite domains. To circumvent this limitation, one can introduce artificial boundaries to the model; this process is also known as spatial truncation. These boundaries, notwithstanding, cause unwanted reflections which defile the response under study [17].

The most straightforward solution is to ensure that the model is large enough to separate unwanted reflections from the studied response in the time domain, which is computationally very expensive for most applications. An alternative solution uses non-reflecting viscous boundary conditions on the finite domain [18] or so-called infinite elements [19]. These formulations mitigate spurious wave reflections at the boundary. However, they cannot trace wave propagation outside the finite computational domain.

The Boundary Element Method (BEM) can accurately model infinite domains without truncation [20]. Its formulation for elastodynamics [21–23] is, therefore, suitable to capture wave propagation towards infinity. The capability of modelling infinite domains arises from its formulation, which uses fundamental solutions that satisfy the radiation condition, allowing for the elimination of domain integrals [24]. By doing so, within the limits of elasticity, the BEM also benefits from a reduced order of discretisation. For this reason, the BEM can efficiently capture wave propagation in tunnelling [25] and earthquake [5,26] simulations. Although the BEM excels in modelling wave propagation in dynamic problems, it is unsuitable for modelling other physical phenomena, such as discontinuities, fracturing and granularity. The previously discussed continuum-based numerical methods, *i.e.* the FEM and the FDM, also have limitations in modelling fracturing and discontinuities.

On the contrary, the Discrete Element Method (DEM) is a numerical method that excels in simulating discontinuities and material fracturing [11]. In the DEM introduced by Cundall and Strack [27], material is represented by an assembly of particles interacting with one another by contact. Cohesive contact models [28] enable the modelling of cohesive materials, such as rock or concrete and their failure under dynamic loading. Donzé et al. [1] applied the DEM to modelling fractures in rock blasting. Regassa et al. [29] used the DEM for simulation of mining-induced rock movements. Fakhimi and Lanari [30] used the bonded-particle DEM model to simulate rock subject to blast loading. Similarly, Song et al. [31] used the DEM to investigate seismic wave propagation excited by an explosion source in a high-steep rock slope site. The deficiency of the DEM due to spurious reflections on the artificial boundary in the simulation of the blast loading can be observed in the latter.

The above review shows that each method excels in capturing a different phenomenon, while real-life applications require simultaneous modelling of various phenomena. Coupling different methods may allow for a more comprehensive numerical model [32,33]. The coupling of numerical methods can be performed in different ways depending on the coupled problem and solution strategy. Different numerical methods are used for various physical fields in multi-field problems and interact in the same domain [34]. In other problems, including the application investigated in this work, different methods are used in different domains. The coupling conditions can be specified at the contact, on the interfacing boundary or an overlapping domain between these domains. Then, the formulation to derive the governing coupled equations can be weak, derived from the minimisation of a specific functional, or strong, where the coupling conditions are explicitly satisfied [35]. In the case of mechanical problems, the coupling conditions are defined by the compatibility and equilibrium conditions.

Numerous publications present the coupling of the DEM with other methods in different domains. The DEM usually models the domain where discontinuous material behaviour is expected, and continuum-based methods represent the remaining domain where the continuous material response can be assumed. Most of these works deal with coupling the DEM and FEM. The work of Oñate and Rojek [36] was among the first to couple the DEM with the FEM by the contact interaction between Discrete Element (DE) particles and Finite Element (FE) elements. Azevedo and Lemos [37] pioneered the interface coupling approach. This formulation, however, produces spurious wave reflection at the interface. Rojek and Oñate [38] identified this reflection and proposed a novel coupling method, extending the work of Xiao and Belytschko [39], with an overlapping region also called the bridging domain. Simultaneously a similar approach, called the Arlequin coupling, was developed by Bauman et al. [40]. Particle rotations were included in the coupling through the bridging domain in [41,42]. Efficient DEM-FEM coupled frameworks with the DEM domain adaptively extended according to material damage and fracture were developed in [32,43–45].

Since the pioneering work of Zienkiewicz et al. [46], several authors developed coupled BEM-FEM schemes. Most of early BEM-FEM models considered static problems [46–48]. Beer [48] proposed the treatment of the BEM region as a large finite element. The pioneering work of Mansur and Brebbia [21] introduced a BEM formulation

for elastodynamics in the time domain. The work of von Estorff and Prabucki [49] used this idea to couple BEM and FEM for transient problems in the time domain. Since the BEM relates displacements to tractions, they used the Newmark method in the FEM to eliminate velocities and accelerations. Later, Yu et al. [50] performed the BEM-FEM coupling using a more numerically stable version of the time domain formulation of the BEM. The work of Soares et al. [51] improved the efficiency of the coupled solution by truncating the BEM convolution. Several works followed in the subsequent years, especially in improving numerical stability [52] and computational efficiency Soares and Mansur [53].

Then, Schanz [23] introduced a formulation for the BEM in dynamics using the Convolution Quadrature Method (CQM) [54]. The main advantage of CQM-BEM is that fundamental solutions are only required in the Laplace domain. Hence, problems involving, for instance, viscoelasticity and poroelasticity can be treated. One limitation is that in the Laplace domain, one cannot filter unwanted frequencies and thus cannot identify natural frequencies, for instance. Moser et al. [55] used Duhamel integrals to derive a dynamic stiffness matrix for the BEM and coupled it with the FEM to model soil–structure interaction. Rüberg and Schanz [56] used the CQM-BEM coupled with the FEM to solve non-conforming interfaces via a Lagrangian formulation. François et al. [57] introduce an iterative coupling scheme to allow different time discretisation in each subdomain.

Only a few attempts have been made to couple the BEM with discontinuous methods. Burczynski et al. [58] coupled the BEM with Molecular Dynamics for static analyses. Mirzayee et al. [59] presented a coupling between the Distinct Element Method and the BEM in the frequency domain. The existing works in the coupled BEM-DEM in the time domain are limited to quasi-static simulations because they apply the static formulation of the BEM [60,61]. To the authors' knowledge, the work of Malinowski et al. [62] is the first attempt to analyse dynamic problems in the time domain using the BEM and the DEM. However, their results rely on a FEM layer between the BEM and the DEM. So, they do not present a direct BEM-DEM coupling. More recently, Barros et al. [63] investigated the BEM-DEM coupling in the time domain for one-dimensional wave propagation in elastic media. Their paper shows that the time step requires careful adjustment as each method has a different stability range.

The current work extends the ideas of Barros et al. [63] to two dimensions and constitutes the first successful attempt to couple BEM and DEM in the time domain for fully dynamic problems. Compared to one dimension, the DEM model becomes more complex in two dimensions as more sophisticated contact laws arise. The BEM also becomes more complicated as the fundamental solutions become more challenging to integrate due to singularities. However, the challenges in coupling lie in more than just the increased complexity of each method. There are also incompatibilities between the methods that do not arise in one-dimensional coupling. One is the equilibrium between the DEM concentrated loads and the BEM tractions. This paper proposes a solution to this incompatibility by transforming BEM tractions into equivalent nodal forces using the principle of virtual displacements. Another incompatibility solved herein regards time integration. Whereas the DEM uses an explicit time integration scheme, the BEM uses the implicit CQM. The solution for this problem is to rewrite DEM equations to make a joint displacement–force equilibrium equation possible. The proposed coupling is defined on the interface level, using a force-based and monolithic formulation, where the arising equations are solved directly, assembling a joint dynamic stiffness matrix.

This paper is structured as follows. Section 2 introduces the reference formulation of the DEM and the BEM. Afterwards, Section 3 discusses the adaptations performed in each method to allow for the coupling. Section 3 introduces the equations that govern the coupled solution. In Section 4, two benchmark problems validate the proposed methodology. Then, a more comprehensive example shows the full capabilities of the proposed model. The DEM captures the fracturing processes due to a sudden load, and the BEM allows the wave to propagate towards infinity. Lastly, Section 5 shows the findings of this work.

2. Numerical framework

2.1. Discrete Element formulation

The DEM is commonly applied to model the dynamics of rigid particle systems. The current work uses the DEM to represent solids as collections of rigid particles. The bonds between particles follow a cohesive contact law to model solid behaviour. Based on Cundall and Strack [27], the formulation used herein uses a set of cylindrical particles to represent the solid. Further, an explicit time integration scheme is adopted that allows for slight overlaps between particles where the contact forces between them are functions of these overlaps.

Newton's second law governs the translational and rotational motions of particle p. It is defined as

$$m_p \ddot{\boldsymbol{u}}_p = \boldsymbol{f}_p(t) \,, \tag{1}$$

$$\mathcal{J}_p \dot{\omega}_p = \mathcal{M}_p(t) \,. \tag{2}$$

In Eq. (1) m_p is the mass, $\ddot{\boldsymbol{u}}_p$ is the acceleration of particle p, and $\boldsymbol{f}_p$ is the resultant force vector acting upon it. In the rotational equation of motion, Eq. (2), $\mathcal{J}_p$ is the moment of inertia, ω_p is the angular velocity of particle p, and $\mathcal{M}_p$ is the resultant moment acting upon it.

Since the problem is in 2D, there are two translational Degrees of Freedom (DOFs) and only a single rotational DOF. Hence, all terms in the rotational equation are scalars with respect to the axis perpendicular to the plane. The displacement $\boldsymbol{u}_p$ of particle p is defined as the difference between its current position and the initial position, *i.e.*, $\boldsymbol{u}_p(t) = \boldsymbol{x}_p(t) - \boldsymbol{x}_p(0)$. Since the initial position is a constant, the velocity and acceleration of particle p are the first and second derivatives of its displacement with respect to time.

Letting $\mathcal{I}_p$ be the set of particles in contact with particle p, the resultant force vector and moment are expressed as

$$\boldsymbol{f}_p(t) = \boldsymbol{f}_{\text{ext},p}(t) + \sum_{i \in \mathcal{I}_p} \boldsymbol{f}_{\text{cont},pi}(t) \,, \tag{3}$$

$$\mathcal{M}_p(t) = \mathcal{M}_{\text{ext},p}(t) + \sum_{i \in \mathcal{I}_p} \mathcal{M}_{\text{cont},pi}(t) \,, \tag{4}$$

where $\boldsymbol{f}_{\text{ext},p}$ and $\mathcal{M}_{\text{ext},p}$ are the external force vector and moment applied to particle p, respectively. In addition, $\boldsymbol{f}_{\text{cont},pi}$ and $\mathcal{M}_{\text{cont},pi}$ are the force vector and moment acting on particle p due to its contact with particle i. Damping terms can be added to Eqs. (3) and (4), but they are not considered in this paper.

The approximate solution of the differential equations, Eqs. (1) and (2), requires a numerical time integration, which in turn requires the discretisation of time in constant time steps of length Δt. Hence, for $n \in \mathbb{N}$, the time is given by $t = n\Delta t$. Consequently, every quantity that depends on time becomes discrete. In the following, the superscript (n) denotes a quantity at time $t = n\Delta t$, *e.g.* $\boldsymbol{u}_p(t = n\Delta t) = \boldsymbol{u}_p^{(n)}$. The time discretisation procedure in the DEM uses the Central Difference (CD) approximation of time derivatives. Hence, the velocity at an intermediate step is given by

$$\dot{\boldsymbol{u}}_p^{\left(n+\frac{1}{2}\right)} = \frac{\boldsymbol{u}_p^{(n+1)} - \boldsymbol{u}_p^{(n)}}{\Delta t} \,, \tag{5}$$

and the acceleration is approximated by

$$\ddot{\boldsymbol{u}}_p^{(n)} = \frac{\dot{\boldsymbol{u}}_p^{\left(n+\frac{1}{2}\right)} - \dot{\boldsymbol{u}}_p^{\left(n-\frac{1}{2}\right)}}{\Delta t} \,. \tag{6}$$

Using the approximations in Eqs. (5) and (6) the numerical time integration used in the DEM is given as follows. For each particle p, compute the acceleration via

$$\ddot{\boldsymbol{u}}_p^{(n)} = \frac{\boldsymbol{f}_p^{(n)}}{m_p} \,, \tag{7}$$

then, calculate the velocity at an intermediate time step through

$$\dot{\boldsymbol{u}}_p^{\left(n+\frac{1}{2}\right)} = \dot{\boldsymbol{u}}_p^{\left(n-\frac{1}{2}\right)} + \ddot{\boldsymbol{u}}_p^{(n)} \Delta t \,, \tag{8}$$

and finally compute the displacement using

$$\boldsymbol{u}_p^{(n+1)} = \boldsymbol{u}_p^{(n)} + \dot{\boldsymbol{u}}_p^{\left(n+\frac{1}{2}\right)} \Delta t \,. \tag{9}$$

This procedure is also known as "leapfrog" integration because displacements and velocities are calculated at different intercalated time steps, half time-step apart, so that they "leapfrog" over each other. Similarly, the rotational motion is described as,

$$\dot{\omega}_p^{(n)} = \frac{\mathcal{M}_p^{(n)}}{\mathcal{J}_p} \,, \tag{10}$$

$$\omega_p^{\left(n+\frac{1}{2}\right)} = \omega_p^{\left(n-\frac{1}{2}\right)} + \dot{\omega}_p^{(n)} \Delta t \,. \tag{11}$$

Note that the actual angle is irrelevant for spherical particles because the inertia tensor is constant in time. Hence, the angular velocity and acceleration are sufficient to represent the rotational motion of the particle.

The explicit time integration is conditionally stable, *i.e.* the time step length Δt is bounded by the critical time step

$$\Delta t \leq \Delta t_{\text{cr}} \,. \tag{12}$$

The critical time step Δt_{cr} in the explicit DEM depends on the stiffnesses of all contacts incident to each particle [64]. Let $\bar{k}_p$ be the equivalent stiffness for particle p, composed of the stiffnesses of all its contacts, and then the global critical time step is defined as the minimum critical time step among all particles

$$\Delta t_{\text{cr}}^{D} = \min_{p} \sqrt{\frac{m_p}{\bar{k}_p}}. \tag{13}$$

Hosn et al. [65] generalised this notion to include rotational DOFs.

The current work uses the cohesive frictional contact model to determine the contact force $\boldsymbol{f}_{\text{cont},pi}^{(n)}$ between two particles p and i. Mohr–Coulomb laws govern the frictional behaviour of the contact model. First, the contact force is decomposed in normal and tangential directions by

$$\boldsymbol{f}_{\text{cont},pi}^{(n)} = f_{n,pi}^{(n)} \boldsymbol{n}_{pi}^{(n)} + f_{s,pi}^{(n)} \boldsymbol{s}_{pi}{}^{(n)} \,, \tag{14}$$

where, $f_{n,pi}^{(n)}$ and $f_{s,pi}^{(n)}$ are the normal and shear contact forces respectively; and $\boldsymbol{n}_{pi}^{(n)}$ and $\boldsymbol{s}_{pi}{}^{(n)}$ are the normal and tangent vectors to the direction of the contact respectively, as illustrated in Fig. 1(a). The cohesive behaviour in the model limits the tensile forces by

$$f_{n,pi}^{(n)} \leq \phi_n \,, \tag{15}$$

where ϕ_n is the cohesion in the normal direction, as depicted by the solid red line in Fig. 2(a). The shear force, in turn, is limited by

$$f_{s,pi}^{(n)} \leq \phi_s - f_{n,pi}^{(n)} \tan\theta_s \,, \tag{16}$$

where ϕ_s is the shear cohesion and θ_s is the friction angle, as depicted as a solid red line in Fig. 2(b). The cohesive bond between particles breaks once the normal or shear force reaches its limit. If future contact forms between those particles, the contact law will follow a purely frictional behaviour represented by the dashed blue line in Figs. 2(a) and 2(b). The Mohr–Coulomb failure criterion emerges from the combination of the normal and the shear behaviours. Fig. 2(c) shows the criterion for cohesive behaviour in a solid red line and the non-cohesive behaviour (*i.e.* after the failure of a cohesive bond) in a dashed blue line.

In Eq. (14), the normal and shear contact forces, $f_{n,pi}^{(n)}$ and $f_{s,pi}^{(n)}$ are calculated incrementally as

$$f_{n,pi}^{(n)} = f_{n,pi}^{(n-1)} + \Delta f_{n,pi}^{(n)} \,, \tag{17}$$

and

$$f_{s,pi}^{(n)} = f_{s,pi}^{(n-1)} + \Delta f_{s,pi}^{(n)} \,. \tag{18}$$

In Eq. (17), the increment on the normal contact force $\Delta f_{n,pi}^{(n)}$ is given by

$$\Delta f_{n,pi}^{(n)} = k_{n,pi} \Delta \delta_{n,pi}^{(n)} \,, \tag{19}$$

where $k_{n,pi}$ is the normal stiffness of the contact (*cf.* Fig. 1(b)), and $\Delta \delta_{n,pi}^{(n)}$ is the increment in the normal relative displacement. Additionally, in Eq. (18), the increment on the shear contact force $\Delta f_{s,pi}^{(n)}$ is given by

$$\Delta f_{s,pi}^{(n)} = k_{s,pi} \Delta \delta_{s,pi}^{(n)} \,, \tag{20}$$

where $k_{s,pi}$ is the shear stiffness of the contact (*cf.* Fig. 1(b)), and $\Delta \delta_{s,pi}^{(n)}$ is the increment in the tangential relative displacement.

According to Cundall and Strack [27], the increments on normal and tangential relative displacements, $\Delta\delta^{(n)}_{n,pi}$ and $\Delta\delta^{(n)}_{s,pi}$, are defined as

$$\Delta\delta^{(n)}_{n,pi} = \left[\left(\dot{\boldsymbol{u}}_p^{\left(n-\frac{1}{2}\right)} - \dot{\boldsymbol{u}}_i^{\left(n-\frac{1}{2}\right)}\right)\cdot \boldsymbol{n}^{(n)}_{pi}\right]\Delta t\,, \tag{21}$$

and

$$\Delta\delta^{(n)}_{s,pi} = \left[\left(\dot{\boldsymbol{u}}_p^{\left(n-\frac{1}{2}\right)} - \dot{\boldsymbol{u}}_i^{\left(n-\frac{1}{2}\right)}\right)\cdot \boldsymbol{s}_{pi}{}^{(n)} - \left(\omega_p^{\left(n-\frac{1}{2}\right)} r_p + \omega_i^{\left(n-\frac{1}{2}\right)} r_i\right)\right]\Delta t\,, \tag{22}$$

where r_p and r_i are the associated particle radii (*cf.* Fig. 1).

The stiffnesses are defined via constitutive models and are generally functions of shape and micro-mechanical material parameters of the particles in contact. This work uses a cohesive frictional contact law, and the stiffnesses are defined with respect to the micro-mechanical Young's moduli E_p, E_i, micro-mechanical Poisson's ratios η_p, η_i and radii r_p, r_i [66]. The normal stiffness is defined as

$$k_{n,pi} = 4\frac{E_p r_p E_i r_i}{E_p r_p + E_i r_i}\,, \tag{23}$$

while the shear stiffness is given by

$$k_{s,pi} = 4\frac{E_p r_p \eta_p E_i r_i \eta_i}{E_p r_p \eta_p + E_i r_i \eta_i}\,. \tag{24}$$

2.2. Boundary Element formulation

The BEM captures the dynamics of continuous media in terms of displacements based on the solution of initial boundary value problems for the underlying partial differential equation. In contrast to other continuum methods, such as the FEM, the BEM requires a discretisation of the associated boundary only. This is achieved by applying the governing differential equation's fundamental solution as the residuals' weighting function.

The BEM formulation presented herein derives from the reciprocal theorem for elastodynamics [22]. The CQM approximates the convolution integrals that arise via weighted sums. The main advantage of the CQM is that it yields a more numerically stable time-stepping algorithm than other BEM formulations [23]. An additional advantage of the CQM is that it only requires the fundamental solution to be explicitly known in the Laplace domain. Thus, a broader range of problems can be solved with the CQM-BEM.

The reciprocal theorem considers two different states: the first state is the domain Ω discretised with the BEM in the coupled analysis, depicted in Fig. 3; the second state consists of an infinite domain with a unit impulse applied at a point $\boldsymbol{\xi}$ at instant $t = 0$. The displacement solution of this second state $\boldsymbol{u}^*$ is known as the fundamental solution.

Applying the reciprocal theorem between those two states and taking into account the properties of the Dirac delta function when integrated, one may write

$$\boldsymbol{C}\boldsymbol{u} = \int_\Gamma \boldsymbol{U}^* \circledast \boldsymbol{t}\,\mathrm{d}\boldsymbol{x} - \int_\Gamma \boldsymbol{T}^* \circledast \boldsymbol{u}\,\mathrm{d}\boldsymbol{x}\,, \tag{25}$$

in which $\boldsymbol{C}(\boldsymbol{\xi})$ is a matrix containing the jump terms that derive from the Dirac delta function, $\boldsymbol{u}(\boldsymbol{\xi}, t)$ and $\boldsymbol{t}(\boldsymbol{\xi}, t)$ are the displacement and traction vectors at a position $\boldsymbol{\xi}$ and time t, respectively, and $\boldsymbol{U}^*(\boldsymbol{\xi}, \boldsymbol{x}, t)$ and $\boldsymbol{T}^*(\boldsymbol{\xi}, \boldsymbol{x}, t)$ are matrices containing the fundamental solutions of displacements and tractions, respectively, for a unit impulse load applied at a point $\boldsymbol{x}$ at instant $t = 0$ and measured at a point $\boldsymbol{\xi}$ at instant t. Furthermore, $\boldsymbol{U}^*$ and $\boldsymbol{T}^*$ are collections of fundamental solutions $\boldsymbol{u}^*$ and $\boldsymbol{t}^*$, for unit impulses applied to each axis. In addition, the operator $\circledast$ indicates a convolution integral given by

$$\left(\boldsymbol{U}^* \circledast \boldsymbol{t}\right)(\boldsymbol{\xi}, \boldsymbol{x}, t) = \int_0^t \boldsymbol{U}^*(\boldsymbol{\xi}, \boldsymbol{x}, t-\tau)\,\boldsymbol{t}(\boldsymbol{x}, \tau)\,\mathrm{d}\tau\,. \tag{26}$$

The extended version of Eq. (25) reads

$$\boldsymbol{C}(\boldsymbol{\xi})\,\boldsymbol{u}(\boldsymbol{\xi}, t) = \int_0^t \int_\Gamma \boldsymbol{U}^*(\boldsymbol{\xi}, \boldsymbol{x}, t-\tau)\,\boldsymbol{t}(\boldsymbol{x}, \tau)\,\mathrm{d}\boldsymbol{x}\,\mathrm{d}\tau - \cancel{\int_0^t} \int_\Gamma \boldsymbol{T}^*(\boldsymbol{\xi}, \boldsymbol{x}, t-\tau)\,\boldsymbol{u}(\boldsymbol{x}, \tau)\,\mathrm{d}\boldsymbol{x}\,\mathrm{d}\tau\,, \tag{27}$$

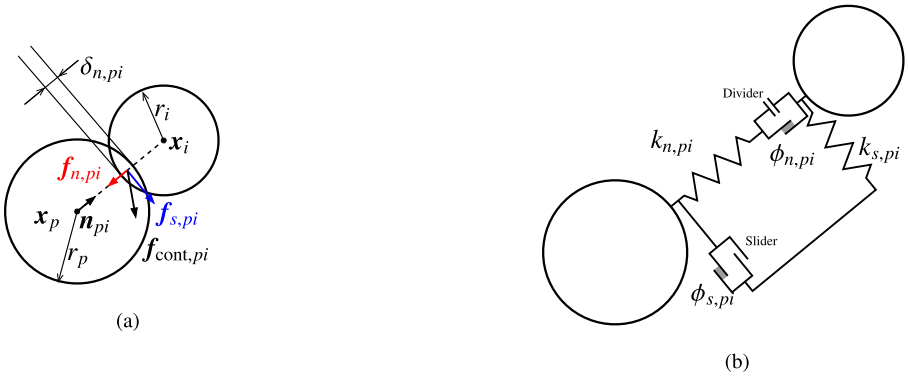

Fig. 1. Contact between two spheres: (a) overlap and contact force and (b) rheological model and its parameters.

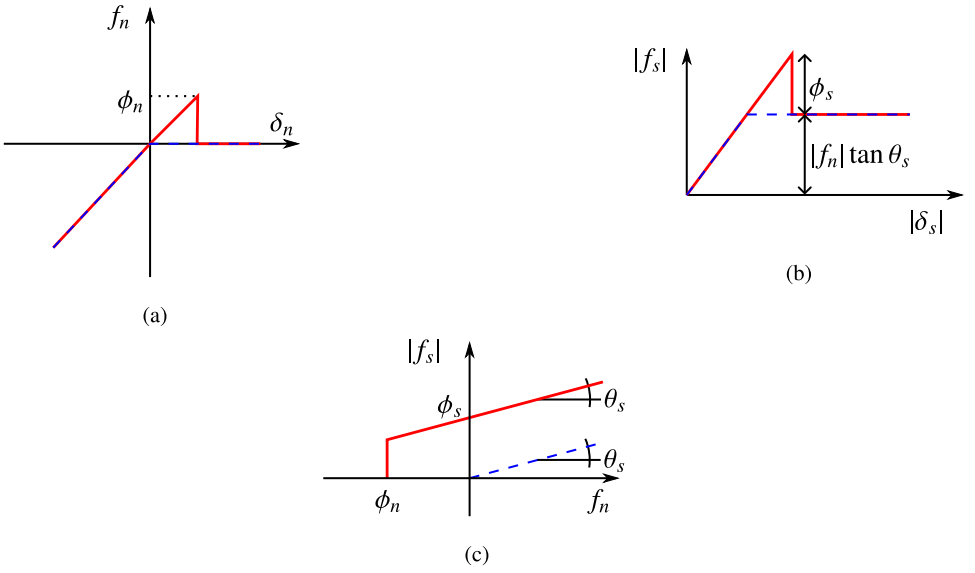

Fig. 2. Cohesive contact law shown in solid red and non-cohesive (after breakage of the cohesive bond) law in dashed blue: (a) normal and (b) shear contact models and (c) Mohr–Coulomb failure criterion. (For interpretation of the references to colour in this figure legend, the reader is referred to the web version of this article.)

where the symbol $⨍$ stands for the finite part of the integral under consideration [67].

It is worth pointing out that Eq. (27) allows one to calculate the displacement of any point in the BEM domain, utilising information on displacements and tractions over the boundary solely. Therefore, when introducing geometric approximations, one only needs to discretise the boundary Γ; no domain discretisation is required. The approximation of the unknowns $\boldsymbol{u}$ and $\boldsymbol{t}$ over the boundary, as illustrated in Fig. 3, are mathematically defined as

$$\boldsymbol{u}\,(\boldsymbol{x},t) = \boldsymbol{\Phi}\,(\boldsymbol{x})\,\boldsymbol{u}_B\,(t)\ , \tag{28}$$

$$\boldsymbol{t}\,(\boldsymbol{x},t) = \boldsymbol{\Psi}\,(\boldsymbol{x})\,\boldsymbol{t}_B\,(t)\ , \tag{29}$$

where $\boldsymbol{u}_B$ is the vector of nodal displacements (the index B indicates that it concerns the BEM region), $\boldsymbol{t}_B$ is the vector of nodal parameters of interpolating tractions within elements, and $\boldsymbol{\Phi}\,(\boldsymbol{x})$ and $\boldsymbol{\Psi}\,(\boldsymbol{x})$ are the interpolating shape-functions for displacements and tractions, respectively.

Substituting the discretisation back at Eq. (25), it becomes

$$\boldsymbol{C}\boldsymbol{u} = \boldsymbol{G} \circledast \boldsymbol{t}_B - \boldsymbol{H} \circledast \boldsymbol{u}_B\ , \tag{30}$$

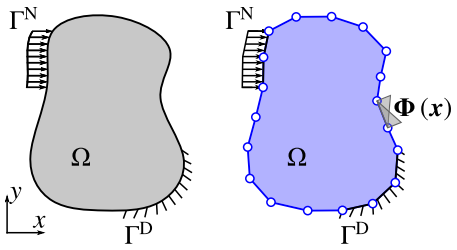

Fig. 3. The domain Ω is discretisation into boundary elements. Γ^{D} and Γ^{N} represent the boundary with Dirichlet and Neumann boundary conditions, respectively. $\boldsymbol{\Phi}(\boldsymbol{x})$ indicates the shape function of a boundary element.

where

$$\boldsymbol{G}(\boldsymbol{\xi}, t) = \int_{\Gamma} \boldsymbol{U}^{*}(\boldsymbol{\xi}, \boldsymbol{x}, t)\, \boldsymbol{\Psi}(\boldsymbol{x})\, \mathrm{d}\boldsymbol{x}\,, \tag{31}$$

and,

$$\boldsymbol{H}(\boldsymbol{\xi}, t) = \int_{\Gamma} \boldsymbol{T}^{*}(\boldsymbol{\xi}, \boldsymbol{x}, t)\, \boldsymbol{\Phi}(\boldsymbol{x})\, \mathrm{d}\boldsymbol{x}\,. \tag{32}$$

Note that, in Eq. (30), while $\boldsymbol{u}_B$ represents the nodal displacements of the DOFs of the entire boundary, $\boldsymbol{u}$ is the displacement of any point in the domain. Thus, if there are m_B nodes in the boundary, $\boldsymbol{u}_B \in \mathbb{R}^{2m_B}$ and $\boldsymbol{u} \in \mathbb{R}^2$ for each point $\boldsymbol{\xi}$ and time t.

Eq. (30) allows for evaluating the displacement at any point of the domain Ω, with geometric approximations only, whereas the solution is still analytical in time. Consequently, a numerical solution for Eq. (30) requires an approximation in time, *i.e.* a time-stepping scheme. That is precisely the role of the CQM. This method approximates the convolution integrals in Eq. (30) by means of weighted sums. The main advantage of this technique is that the weights depend only on the time step Δt and the fundamental solution in the Laplace domain. Since the fundamental solution in the time domain is not required, the CQM can solve a broader variety of problems [23]. Applying the CQM to Eq. (30) it becomes

$$\boldsymbol{C}\boldsymbol{u}^{(n+1)} = \sum_{k=0}^{n+1} \boldsymbol{G}^{(n+1-k)} \boldsymbol{t}_B^{(k)} - \sum_{k=0}^{n+1} \boldsymbol{H}^{(n+1-k)} \boldsymbol{u}_B^{(k)}\,. \tag{33}$$

The BEM formulation's final step consists of taking the limit of Eq. (33) as the point $\boldsymbol{\xi}$ tends to each point $\boldsymbol{x}$ on the boundary. This process is known as collocation and allows one to write the final equation of the CQM-BEM

$$\sum_{k=0}^{n+1} \boldsymbol{H}_B^{(n+1-k)} \boldsymbol{u}_B^{(k)} = \sum_{k=0}^{n+1} \boldsymbol{G}_B^{(n+1-k)} \boldsymbol{t}_B^{(k)}\,, \tag{34}$$

where $\boldsymbol{H}_B^{(n+1-k)}$ and $\boldsymbol{G}_B^{(n+1-k)}$ are matrices that come from the collocation process. Note that, $\boldsymbol{G}_B$ has only terms from $\boldsymbol{G}$ as $\boldsymbol{\xi} \to \boldsymbol{x}$, $\forall \boldsymbol{x} \in \Gamma$, and, $\boldsymbol{H}_B$ has terms from $\boldsymbol{H}$ and $\boldsymbol{C}$.

After determining all the quantities in the boundary, the BEM allows for evaluating results at any point inside the domain Ω. The evaluation of displacements at internal points also relies on Eq. (33). In the case of internal points, the matrix $\boldsymbol{C}$ becomes the identity matrix. Hence, the evaluation of displacements at internal points follows

$$\boldsymbol{u}_{\mathrm{int}}^{(n+1)} = \sum_{k=0}^{n+1} \boldsymbol{G}_{\mathrm{int}}^{(n+1-k)} \boldsymbol{t}_B^{(k)} - \sum_{k=0}^{n+1} \boldsymbol{H}_{\mathrm{int}}^{(n+1-k)} \boldsymbol{u}_B^{(k)}\,. \tag{35}$$

3. Coupling

A monolithic and direct formulation is applied to couple the BEM and the DEM. Two incompatibilities between the distinct methods must be solved to perform this coupling. The first incompatibility is that the BEM deals with tractions on the boundary (see Eq. (34)) rather than with concentrated loads as the DEM. The second incompatibility

is that velocities and accelerations do not appear in Eq. (34). Instead, the inertial terms are considered implicitly in the $\boldsymbol{H}$ and $\boldsymbol{G}$ matrices.

Given these two incompatibilities, the successful coupling between those methods requires few adaptations in their classical formulation. The goal is to write equilibrium equations correlating nodal forces and displacements through dynamic stiffness matrices for both methods. In the BEM, equivalent nodal forces are encountered by applying the principle of virtual displacements. In the DEM, the central difference approximation is rewritten to find the sought equation.

3.1. Adapting the Boundary Element Method

The adaption in the BEM starts by isolating the tractions at the time step $n+1$, *i.e.*

$$\boldsymbol{t}_B^{(n+1)} = \left(\boldsymbol{G}_B^{(0)}\right)^{-1} \boldsymbol{H}_B^{(0)} \boldsymbol{u}_B^{(n+1)} + \left(\boldsymbol{G}_B^{(0)}\right)^{-1} \left(\sum_{k=0}^{n} \boldsymbol{H}_B^{(n+1-k)} \boldsymbol{u}_B^{(k)} - \boldsymbol{G}_B^{(n+1-k)} \boldsymbol{t}_B^{(k)} \right) . \tag{36}$$

Then the principle of virtual displacements is applied to write an equilibrium relationship between tractions and equivalent nodal forces as $\boldsymbol{f}_B^{(n+1)} = \boldsymbol{N}\boldsymbol{t}_B^{(n+1)}$. Hence, these loads can be written in terms of displacements as

$$\boldsymbol{f}_B^{(n+1)} = \boldsymbol{K}_B \boldsymbol{u}_B^{(n+1)} - \boldsymbol{h}_B^{(n+1)} \tag{37}$$

where $\boldsymbol{K}_B$ is the dynamic stiffness matrix of the BEM region given by

$$\boldsymbol{K}_B = \boldsymbol{N} \left(\boldsymbol{G}_B^{(0)}\right)^{-1} \boldsymbol{H}_B^{(0)} \tag{38}$$

and $\boldsymbol{h}_B^{(n+1)}$ is the vector of loads acting at time step $n+1$ due to the history of analysis. $\boldsymbol{h}_B^{(n+1)}$ is defined by

$$\boldsymbol{h}_B^{(n+1)} = \boldsymbol{N} \left(\boldsymbol{G}_B^{(0)}\right)^{-1} \left(\sum_{k=0}^{n} \boldsymbol{G}_B^{(n+1-k)} \boldsymbol{t}_B^{(k)} - \boldsymbol{H}_B^{(n+1-k)} \boldsymbol{u}_B^{(k)} \right) \tag{39}$$

only including terms computed before time step $n+1$. Eq. (37) can then be condensed to relate only DOFs at the interface. In the BEM formulation, note that displacements refer to the initial configuration.

3.2. Adapting the Discrete Element Method

The procedure described in Section 2 solves the motion of the particles. As aforementioned, the equations that govern the motion of the particles at the interface need to be rewritten to allow for coupling. In the current formulation, the rotations of the particles at the interface are not coupled with the displacement field of the BEM and the stiffnesses between them need to be changed to compensate for overlapping with the BEM domain. To adapt the DEM formulation for coupling, a direct approximation of the acceleration in terms of displacements is sought instead of the approach using the velocity. One can achieve this by substituting Eq. (5) for $n+\frac{1}{2}$ and $n-\frac{1}{2}$ in Eq. (6), which gives

$$\frac{\boldsymbol{f}_p^{(n)}}{m_p} = \ddot{\boldsymbol{u}}_p^{(n)} = \frac{\boldsymbol{u}_p^{(n+1)} - 2\boldsymbol{u}_p^{(n)} + \boldsymbol{u}_p^{(n-1)}}{\Delta t^2} , \tag{40}$$

which can be rearranged as

$$\boldsymbol{f}_p^{(n)} = \boldsymbol{u}_p^{(n+1)} \frac{m_p}{\Delta t^2} - \left(2\boldsymbol{u}_p^{(n)} - \boldsymbol{u}_p^{(n-1)}\right) \frac{m_p}{\Delta t^2} . \tag{41}$$

Grouping Eq. (41) for all particles p at the interface, the system of equilibrium equations is defined similarly to Eq. (37) by

$$\boldsymbol{f}_D^{(n+1)} = \boldsymbol{K}_D \boldsymbol{u}_D^{(n+1)} - \boldsymbol{h}_D^{(n+1)} . \tag{42}$$

The index D indicates the DEM region, and $\boldsymbol{f}_D^{(n+1)}$ is a null vector, which means that only the history load vector causes motion in the particles. That is due to the applied explicit time integration. Moreover, the dynamic stiffness matrix is defined by

$$\boldsymbol{K}_D = \text{diag} \left\{ \frac{m_1}{\Delta t^2}, \frac{m_1}{\Delta t^2}, \frac{m_2}{\Delta t^2}, \frac{m_2}{\Delta t^2}, \ldots, \frac{m_P}{\Delta t^2}, \frac{m_P}{\Delta t^2} \right\} , \tag{43}$$

where P is the number of particles at the interface. The history load vector reads

$$\boldsymbol{h}_D^{(n+1)} = \boldsymbol{f}_D^{(n)} + \boldsymbol{K}_D \left(2\boldsymbol{u}_D^{(n)} - \boldsymbol{u}_D^{(n-1)}\right) . \tag{44}$$

3.3. Assembling coupled equations

Lastly, the total load acting upon the DOFs on the interface are computed via

$$\boldsymbol{f}^{(n+1)} = \boldsymbol{f}_B^{(n+1)} + \boldsymbol{f}_D^{(n+1)} = \boldsymbol{K}_B \boldsymbol{u}_B^{(n+1)} - \boldsymbol{h}_B^{(n+1)} + \boldsymbol{K}_D \boldsymbol{u}_D^{(n+1)} - \boldsymbol{h}_D^{(n+1)} . \tag{45}$$

Since compatibility requires the equality $\boldsymbol{u}_B^{(n+1)} = \boldsymbol{u}_D^{(n+1)} = \boldsymbol{u}^{(n+1)}$ at the interface, it yields

$$\boldsymbol{f}^{(n+1)} = \boldsymbol{K}\boldsymbol{u}^{(n+1)} - \boldsymbol{h}^{(n+1)} . \tag{46}$$

in which

$$\boldsymbol{f}^{(n+1)} = \boldsymbol{f}_B^{(n+1)} , \tag{47}$$

since $\boldsymbol{f}_D^{(n+1)} = \boldsymbol{0}$,

$$\boldsymbol{h}^{(n+1)} = \boldsymbol{h}_B^{(n+1)} + \boldsymbol{h}_D^{(n+1)} , \tag{48}$$

and

$$\boldsymbol{K} = \begin{bmatrix} (k_{\mathrm{B}})_{1,1} + \frac{m_1}{\Delta t^2} & (k_{\mathrm{B}})_{1,2} & (k_{\mathrm{B}})_{1,3} & (k_{\mathrm{B}})_{1,4} & \cdots & (k_{\mathrm{B}})_{1,2P-1} & (k_{\mathrm{B}})_{1,2P} \\ (k_{\mathrm{B}})_{2,1} & (k_{\mathrm{B}})_{2,2} + \frac{m_1}{\Delta t^2} & (k_{\mathrm{B}})_{2,3} & (k_{\mathrm{B}})_{2,4} & \cdots & (k_{\mathrm{B}})_{2,2P-1} & (k_{\mathrm{B}})_{2,2P} \\ (k_{\mathrm{B}})_{3,1} & (k_{\mathrm{B}})_{3,2} & (k_{\mathrm{B}})_{3,3} + \frac{m_2}{\Delta t^2} & (k_{\mathrm{B}})_{3,4} & \cdots & (k_{\mathrm{B}})_{3,2P-1} & (k_{\mathrm{B}})_{3,2P} \\ (k_{\mathrm{B}})_{4,1} & (k_{\mathrm{B}})_{4,2} & (k_{\mathrm{B}})_{4,3} & (k_{\mathrm{B}})_{4,4} + \frac{m_2}{\Delta t^2} & \cdots & (k_{\mathrm{B}})_{4,2P-1} & (k_{\mathrm{B}})_{4,2P} \\ \vdots & \vdots & \vdots & \vdots & \ddots & \vdots & \\ (k_{\mathrm{B}})_{2P-1,1} & (k_{\mathrm{B}})_{2P-1,2} & (k_{\mathrm{B}})_{2P-1,3} & (k_{\mathrm{B}})_{2P-1,4} & \cdots & (k_{\mathrm{B}})_{2P-1,2P-1} + \frac{m_P}{\Delta t^2} & (k_{\mathrm{B}})_{2P-1,2P} \\ (k_{\mathrm{B}})_{2P,1} & (k_{\mathrm{B}})_{2P,2} & (k_{\mathrm{B}})_{2P,3} & (k_{\mathrm{B}})_{2P,4} & \cdots & (k_{\mathrm{B}})_{2P,2P-1} & (k_{\mathrm{B}})_{2P,2P} + \frac{m_P}{\Delta t^2} \end{bmatrix} \tag{49}$$

4. Results

4.1. Finite rod under Heaviside load

Fig. 4(a) shows a finite cantilever rod with a total length of $L = 2\,\mathrm{m}$, a cross-section area of $A = 0.25\,\mathrm{m}^2$, a Young's modulus of $E = 210\,\mathrm{MPa}$ and a mass density of $\rho = 7.85\,\mathrm{t/m}^3$. The rod is subjected to a Heaviside load $P(t) = P_0 H(t)$ on the free end, where $P_0 = 21\,\mathrm{kN}$ is the maximum value of the load, as shown in Fig. 4(b). This example is a classical benchmark test, often used to validate numerical frameworks in elastodynamics. The Poisson's ratio of the material does not influence the one-dimensional analytical solution; thus, it will be assumed $\nu = 0$. Moreover, the thickness t_h is assumed to be unitary; therefore, the height of the rod becomes $h = 25\,\mathrm{cm}$. The observation extends to 5 ms.

The rod is modelled using both regular orthogonal and irregular particle assemblies, as shown in Figs. 4(c) and 4(d), respectively. The generation of irregular assemblies assumes a reference particle size D_{ref} and attributes a uniform probability distribution between the minimum and the maximum particle sizes, D_{min} and D_{max}. The minimum and maximum particle sizes are 25 % apart from the reference values, hence, $D_{\mathrm{min}} = 0.75 D_{\mathrm{ref}}$ and $D_{\mathrm{max}} = 1.25 D_{\mathrm{ref}}$. Since the generation of the irregular assemblies follows a stochastic process, five different assemblies were generated for each reference particle size considered, $D_{\mathrm{ref}} \in \{12.5\,\mathrm{cm}, 5\,\mathrm{cm}, 2.5\,\mathrm{cm}, 1.25\,\mathrm{cm}\}$. In generating the particle assemblies, the particles on the interface were kept fixed so that their centres would coincide with the BEM nodes. As mentioned in Section 3.2, the rotations of particles at the interface are not coupled with the BEM displacement field. Initial numerical simulations, in which the rotational DOF of these particles was tested as both fixed and free, exhibit no significant discrepancy. Therefore, all subsequent results were obtained by assuming fixed rotations.

Since the goal is to model the continuum behaviour within the DEM region as well as possible, the associated material properties must be carefully calibrated. Firstly, one calculates α_p, the percentage of the mass of particle p

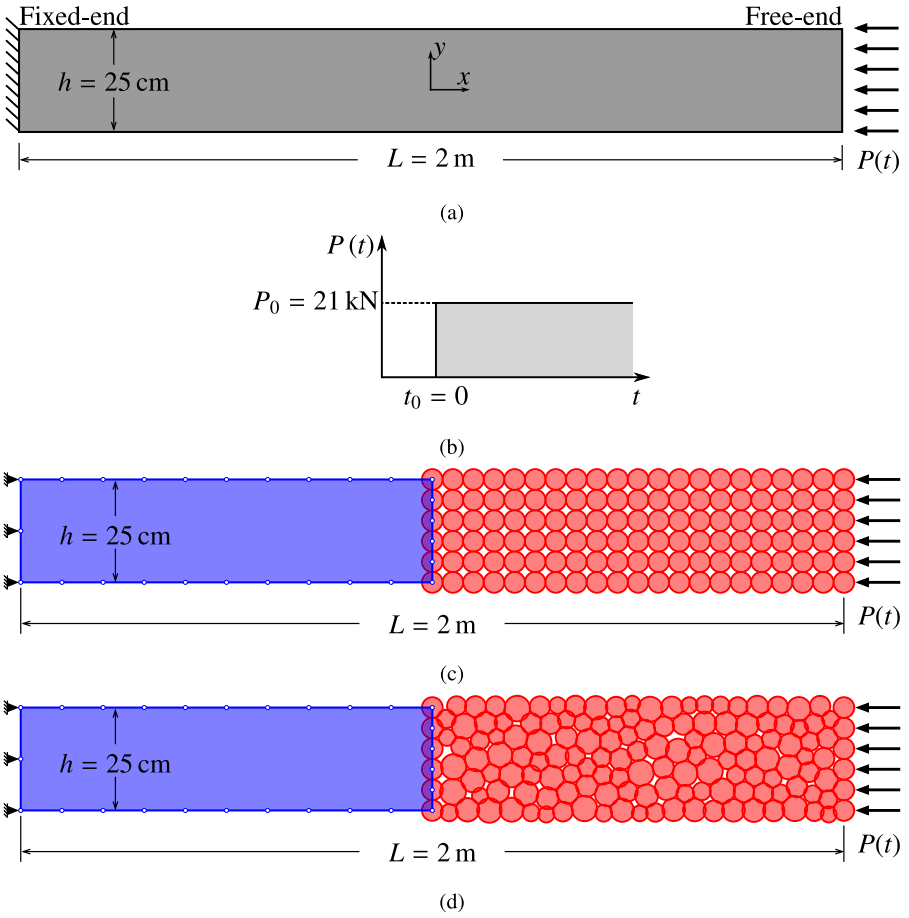

Fig. 4. Homogeneous rod under Heaviside compression load: (a) conceptual model, (b) distribution of load over time, (c) regular orthogonal DEM pack using particle size $D = 5\,\text{cm}$, and (d) irregular DEM pack using particle size $D = 5\,\text{cm} \pm 25\,\%$.

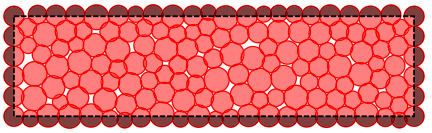

Fig. 5. Percentage of mass inside the original rod domain.

inside the original rod domain. Fig. 5 shows the same assembly as Fig. 4(d) overlaid by the original rod domain. The darker areas are to be discarded from the mass of the particles since they are outside the rod domain. For instance, for particles at the corners, it yields $\alpha_p = 0.25$. Moreover, the effective mass density for the DEM region is given by

$$\overline{\rho} = \rho \frac{L h t_h}{\sum_{p=0}^{m} \alpha_p V_p}\,, \tag{50}$$

where m is the number of particles and V_p is the volume of particle p. Eq. (50) is based on the equality of the particulate and the mass of the rod.

Secondly, the elastic micro-mechanical parameters must be calibrated. The Young's modulus of each particle p is given by

$$E_p = E f_E \alpha_p\,, \tag{51}$$

Table 1
Calibrated elastic parameters f_E for rod model.

D_{ref}	Packing				
	I	II	III	IV	V
12.5	15.304	15.401	15.582	13.776	16.942
5	33.206	30.543	32.394	33.465	31.502
2.5	56.434	56.635	54.223	54.996	55.523
1.25	108.201	108.201	109.050	107.614	107.948

where f_E is a global parameter that has to be calibrated. The parameter α_p accounts for the part of the particles lying outside the DEM domain. The contact stiffnesses are adjusted accordingly (see Eqs. (23) and (24)). The microscopic Poisson's ratio $\eta = 1.0$ is assumed to represent the macroscopic Poisson's ratio of $\nu = 0$. Additionally, to capture purely elastic behaviour, the normal and shear cohesions are considered infinite, *i.e.* $\phi_n = \phi_s = \infty$. The calibrations were performed using GrainLearning [68,69], aiming to fit the numerical result as closely as possible to the analytical one. The observation data consists only of the analytical displacement at the end node in the time domain. A single calibration was performed for each assembly. Table 1 shows the calibrated parameters for each particle size and packing adopted.

Figs. 6 and 7 show the analytic solution and numerical prediction calculated using the numerical coupled BEM-DEM solution. In the latter, the plotted displacement is the average of the displacements of particles in the cross-section corresponding to that node. In these graphs, the solid lines represent the analytical solution, the displacement of the free-end is shown in blue, and the interface displacement is depicted in yellow. The dash-dotted lines show the numerical predictions using a regular orthogonal DEM assembly. The associated green line corresponds to the predicted displacement of the free end, and the red one corresponds to the expected interface displacement. The dashed lines represent the averaged numerical predictions of irregular assemblies with the same reference particle size, *i.e.* the mean of different particle configurations are considered. The dashed pink and brown lines show the average displacement of the free end and at the interface. In addition, the shaded area around the dashed lines represents the maximum and minimum displacements observed at a given time among all assemblies.

Visual analysis of Figs. 6 and 7 indicates that as the particle size decreases, not only the numerical prediction approximates the analytical solution better, but also that the dispersion of results for irregular assemblies reduces. Such effect is further exploited in Fig. 8, where the normalised absolute difference between the analytical response u and the numerical prediction d is plotted as colour bars. Once again, the numerical response is taken as the average across the cross-section. The absolute difference is normalised by the analytical solution for statics. This plot sheds light on how the error can be decreased by refining the discretisation in both domains.

4.2. Cylindrical cavity in infinite space under uniform pressure

Another commonly used benchmark test in elastodynamics is the cavity example. It consists of a cylindrical cavity of radius $R_1 = 1.0\,\text{m}$ embedded in an infinite space, as shown in Fig. 9(a). The cavity is composed of a material whose macroscopic parameters are: Young's modulus $E = 100\,\text{kPa}$, Poisson's ratio $\nu = 0$, and mass density $\rho = 1.0\,\text{t/m}^3$. The problem is assumed to have a unitary thickness, *i.e.*, $t_h = 1.0\,\text{m}$. Fig. 9(a) shows the internal pressure $p\,(t)$ applied to the cavity. The magnitude of the pressure over time is given by a Heaviside function, *i.e.*, $p\,(t) = p_0 H\,(t)$, where $p_0 = 1.0\,\text{kN/m}^2$, as shown in Fig. 9(b). Because of the infinite nature of the problem, the use of the BEM becomes even more advantageous than in the rod example. Therefore, the DEM domain is set to be a finite cylinder with internal radius $R_1 = 1.0\,\text{m}$ and external radius $R_2 = 2.0\,\text{m}$. The remaining infinite domain of the problem is modelled with the BEM.

This problem is analysed using irregular particle assemblies. The reference diameters considered are $D_{\text{ref}} \in \{10, 15, 20, 25, 30, 35\}\,\text{cm}$. The particle sizes are uniformly distributed for each reference diameter between $0.75 D_{\text{ref}}$ and $1.25 D_{\text{ref}}$. For each reference diameter, three irregular assemblies were generated to allow for an analysis of the dispersion of the results. Figs. 9(c) and 9(d) show the irregular assemblies obtained for $D_{\text{ref}} = 35\,\text{cm}$ and $D_{\text{ref}} = 10\,\text{cm}$ respectively.

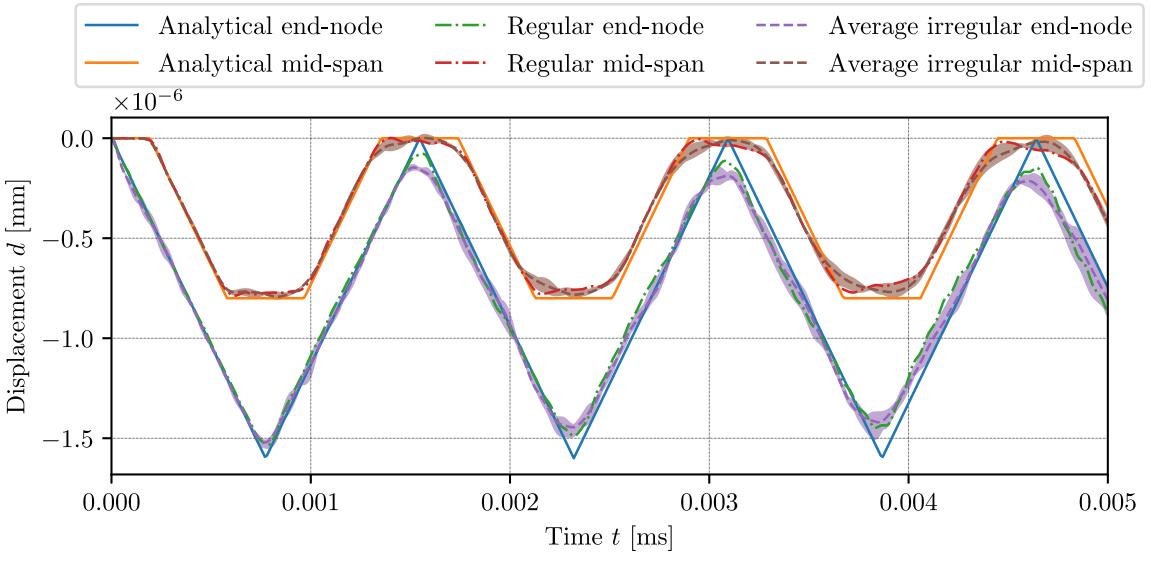

(a)

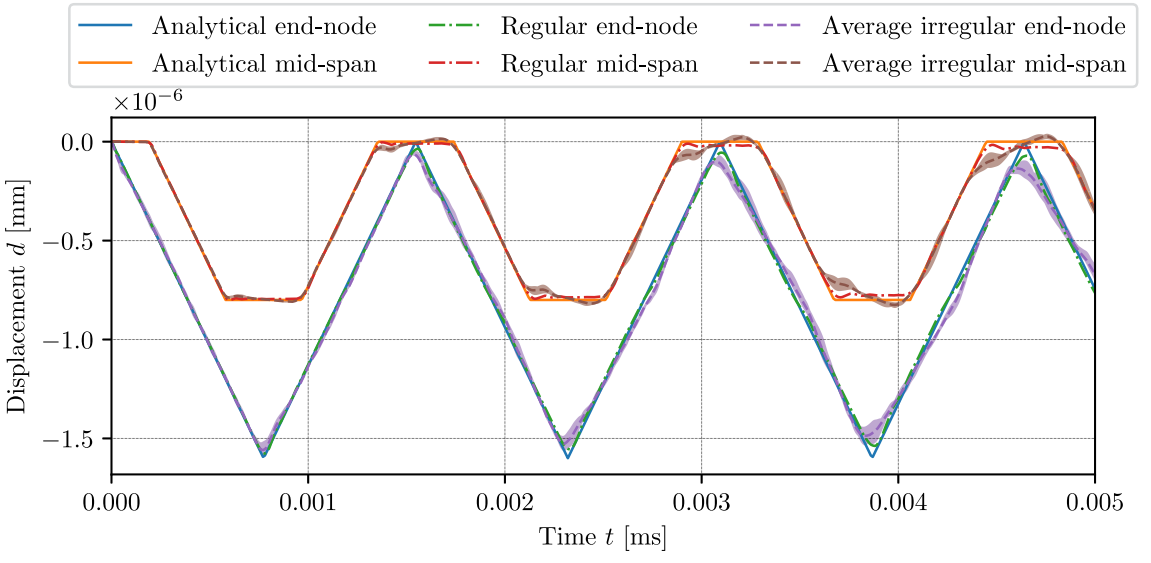

(b)

Fig. 6. Analytical and numerical displacement at free-end of rod using: (a) particle size $D_{\text{ref}} = 12.5\,\text{cm}$ and (b) particle size $D_{\text{ref}} = 5\,\text{cm}$. (For interpretation of the references to colour in this figure legend, the reader is referred to the web version of this article.)

A mass correction similar to Section 4.1 needs to be applied. It can be noticed in Fig. 9(c), for instance, that approximately half of the particles in the cavity are inside the domain of the problem. Similarly, the particles at the interface have one-half in the DEM domain and the other half in the BEM domain. Hence, a factor $\alpha_p = 0.5$ is assigned to those particles, while for the other particles, this factor is $\alpha_p = 1.0$. The mass density of the particles is defined by equating the total mass of the assembly to the macroscopic mass of the cylinder, hence,

$$\overline{\rho} = \rho \frac{t_h \pi \left(R_2^2 - R_1^2\right)}{\sum_{p=0}^{m} \alpha_p V_p}, \tag{52}$$

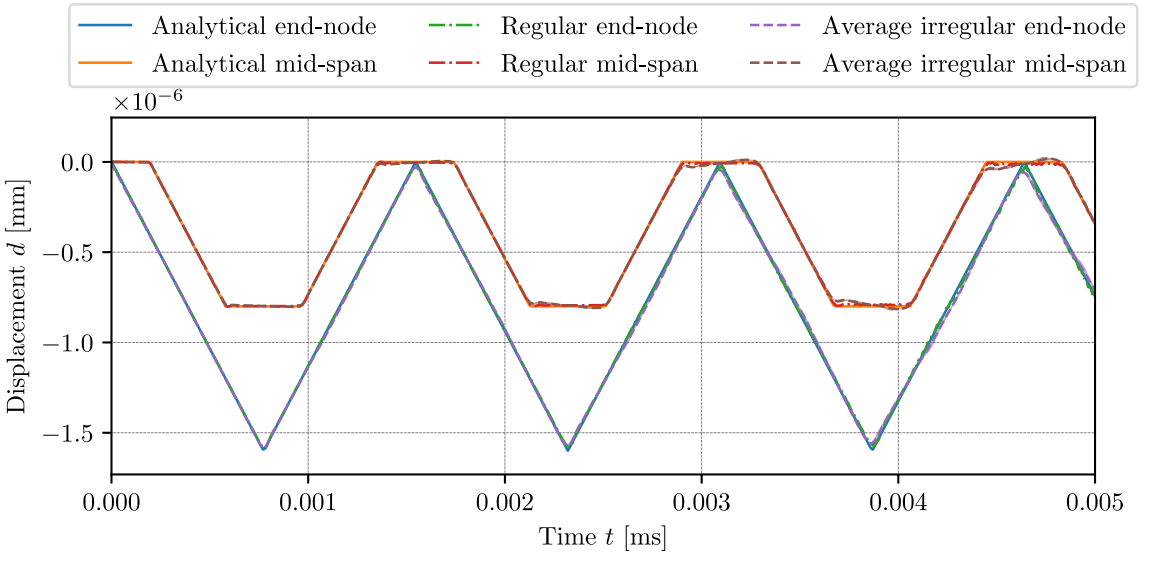

(a)

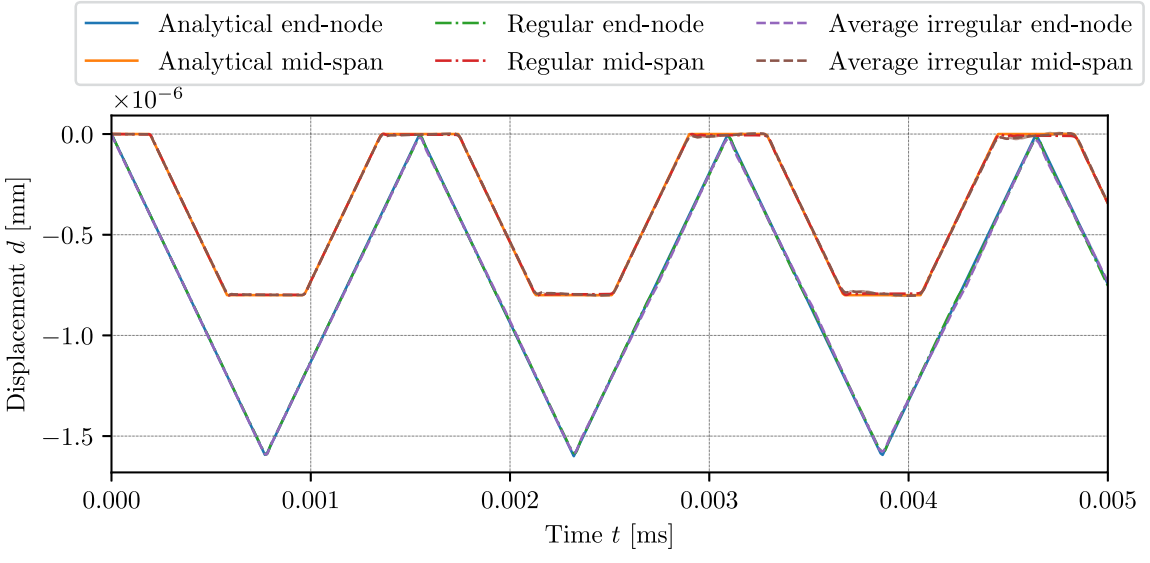

(b)

Fig. 7. Analytical and numerical displacement at free-end of rod using: (a) particle size $D_{\text{ref}} = 2.5\,\text{cm}$ and (b) particle size $D_{\text{ref}} = 1.25\,\text{cm}$. (For interpretation of the references to colour in this figure legend, the reader is referred to the web version of this article.)

where V_p is the volume of the pth particle. Again, calibrations are required to determine the microscopic parameters to yield the desired macroscopic behaviour for each generated particle assembly. The microscopic Poisson's ratio is set to $\eta = 1.0$ to represent the macroscopic $\nu = 0$, and the normal and shear cohesions are set to $\phi_n = \phi_s = \infty$ to capture purely elastic behaviour. The only parameter left is the microscopic Young's modulus, which is the multiplication of the macroscopic Young's modulus by a factor f_E. This factor is calibrated, as previously, using GrainLearning [68,69]. The calibrated factors for each assembly are displayed in Table 2.

To assess the accuracy of the proposed coupling approach, the displacements of three points, A $(1, 0)$, B $(2, 0)$ and C $(4, 0)$, are investigated. Point A is at the cavity, point B at the interface, and point C is inside the BEM

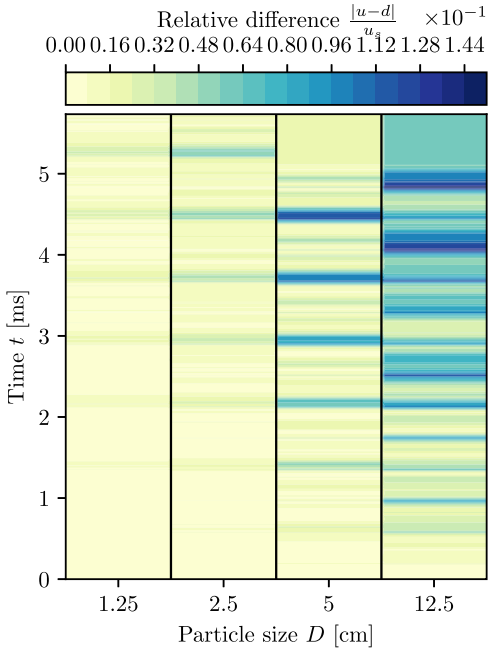

Fig. 8. Error in free-end displacement normalised by static displacement.

Table 2
Calibrated elastic parameters f_E for cavity model.

D_{ref}	Packing		
	I	II	III
35	4.719	3.990	4.694
30	4.493	4.171	5.931
25	6.816	5.815	5.747
20	9.050	10.150	7.941
15	10.141	10.448	10.704
10	15.866	14.702	14.188

domain (*i.e.* far field). Reference solutions for the displacements of points A and C are available in [55]. They are semi-analytical responses obtained via the CQM using the analytical solution in the Laplace domain and a fine discretisation in time. Figs. 10 to 12 show the numerical predictions for the displacements of points A, B and C over time. The solid lines represent the average among all generated irregular assemblies in those figures. The blue line represents the displacement of point A, the yellow line represents the displacement of point B, and the green line represents the displacement of point C. The shaded area around them covers the maximum and minimum values observed among all assemblies. The dashed lines represent the reference solutions. The red and purple lines refer to points A and C, respectively.

By analysing Figs. 10 to 12, one can notice that as the particle size decreases, the numerical predictions approach the reference semi-analytical solution. In addition, the dispersion of prediction over different assemblies becomes slimmer, and the shaded area is practically unnoticeable behind its corresponding solid line. This pattern is also observed in the rod example in Section 4.1. Hence, the coupled behaviour is the same for both benchmarks, which validates the effectiveness of the newly proposed method.

Fig. 13 depicts the errors observed in the displacement of point A for different particle sizes. One can infer that the overall error tends to decay as the particle size decreases. Even though there are some localised parts where the error is higher, the overall error decays. One might expect localised high errors to appear when comparing a discontinuous numerical response to a semi-analytical solution obtained with the continuum hypotheses.

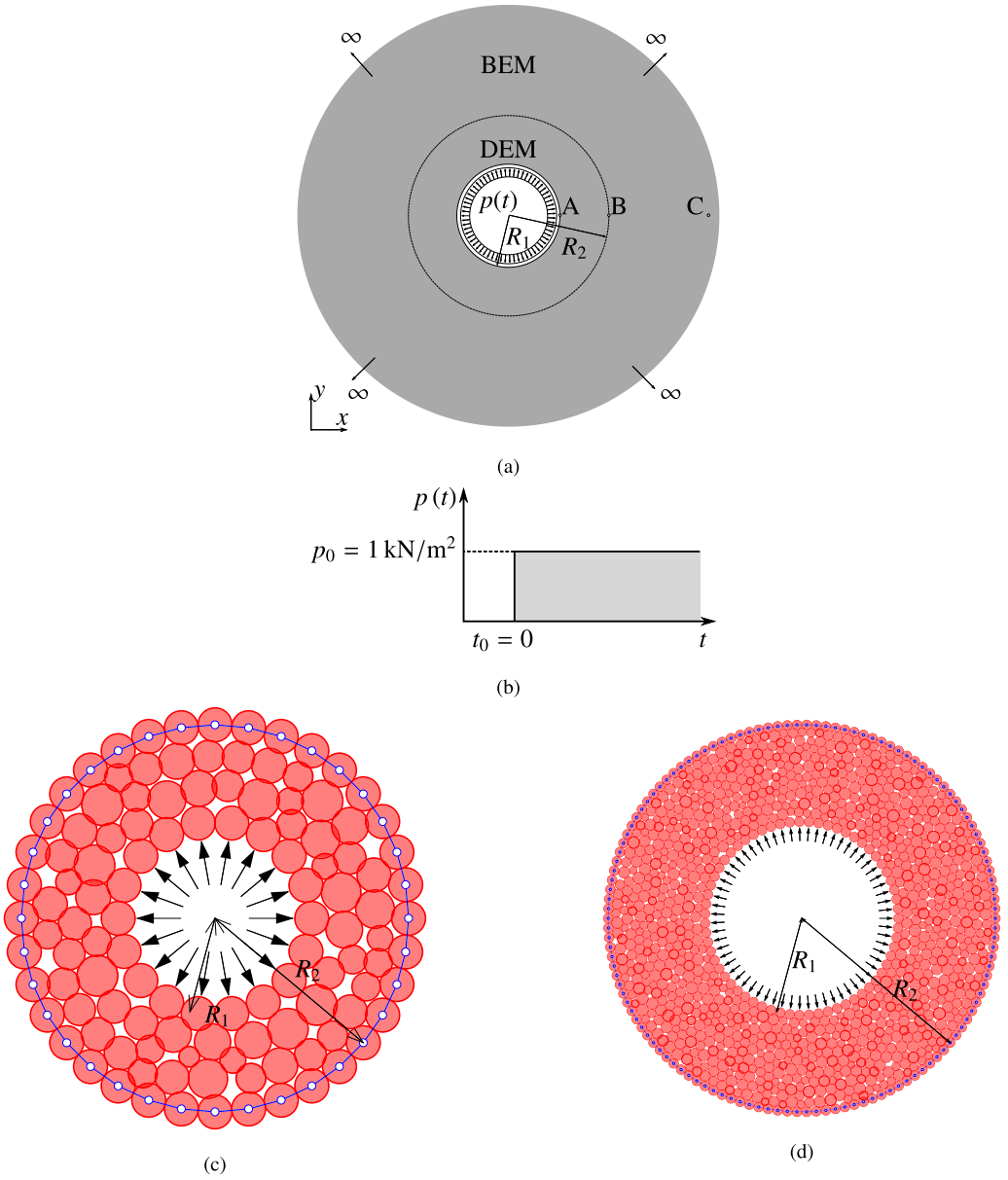

Fig. 9. Cylindrical cavity in infinite space under uniform pressure: (a) conceptual model, (b) distribution of pressure over time, (c) irregular DEM pack using particle size $D = 35\,\text{cm} \pm 25\,\%$, and (d) irregular DEM pack using particle size $D = 10\,\text{cm} \pm 25\,\%$.

Lastly, Fig. 14 shows the velocities of each particle in the numerical solution obtained using a particle assembly with reference particle size $D_{\text{ref}} = 10\,\text{cm}$. The figures capture the velocities at different instants so that the wave propagation is seen. The data in Fig. 14 is consistent with the data in Fig. 12(b). After 300 ms, the displacements tend to a plateau, so the velocities tend to zero. Moreover, Fig. 14 evidences that no significant spurious wave reflection occurs at the interface, *i.e.* the wave is travelling from the DEM domain into the BEM domain.

4.3. Cavity fracturing under impulse load

The last example is a cavity with the same geometry as in Fig. 9(a) fracturing under a rectangular impulse load which vanishes after 10 ms, as shown in Fig. 15. This example has the same elastic parameters as the one in

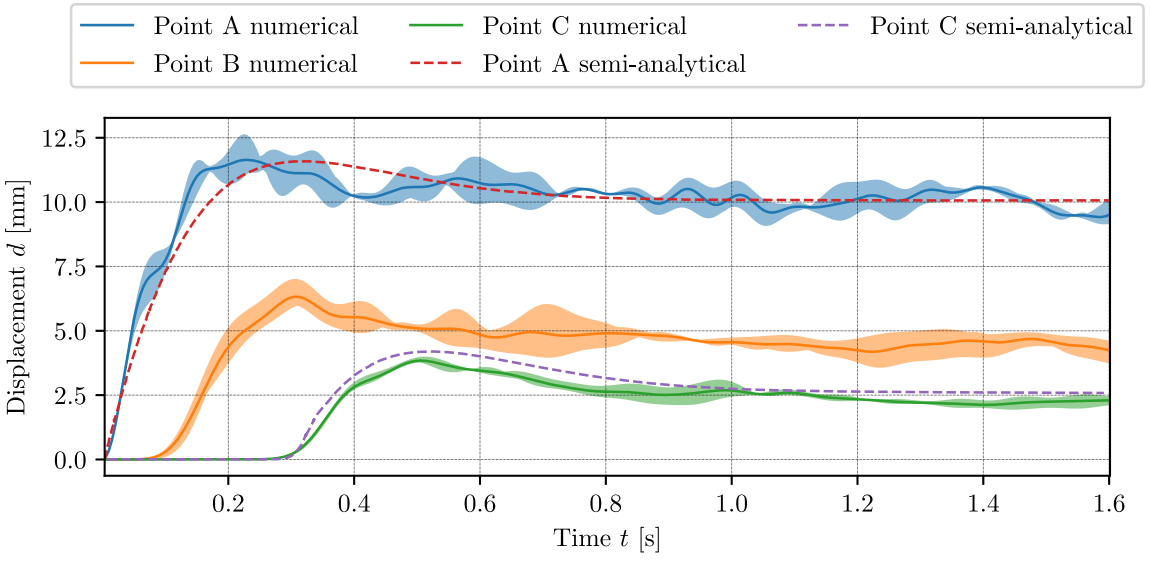

(a)

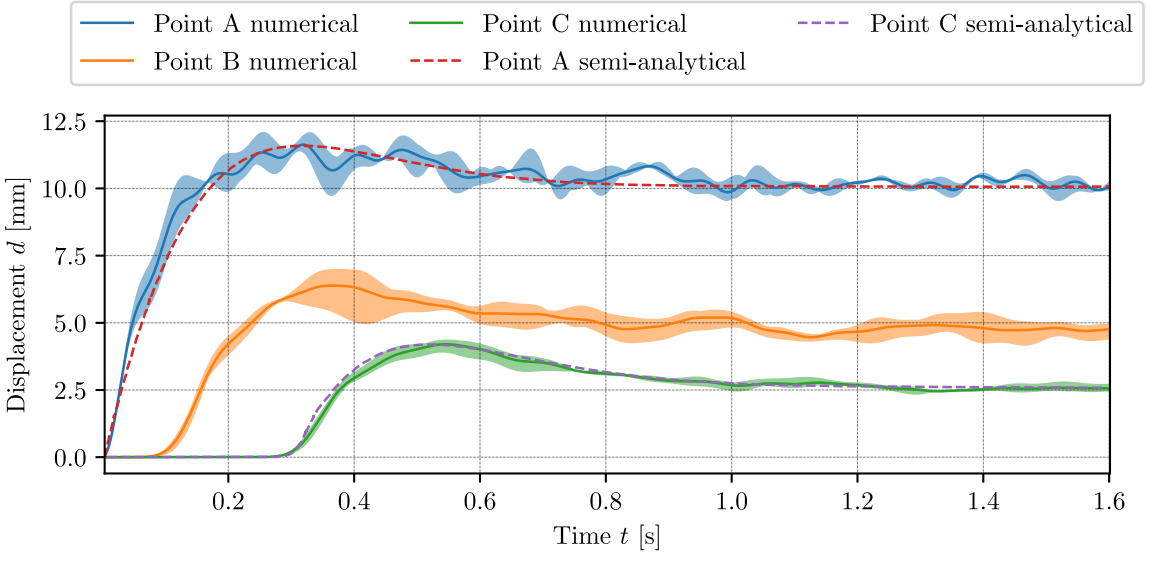

(b)

Fig. 10. Analytical and numerical displacement at cavity using: (a) particle size $D_{\text{ref}} = 35\,\text{cm}$ and (b) particle size $D_{\text{ref}} = 30\,\text{cm}$. (For interpretation of the references to colour in this figure legend, the reader is referred to the web version of this article.)

Section 4.2. In order to allow for fracture behaviour, the normal cohesion is set to $\phi_n = 110\,\text{kN}$ and $\phi_n/\phi_s = 1/3$ as used by Donzé et al. [1]. Fig. 16 shows how the wave propagates within the domain. Similarly, as in the previous example, it can be seen that the wave is travelling from the DEM domain into the BEM domain with no reflection at the interface.

Fig. 17 shows the damage each particle has sustained. The damage is calculated as the ratio between the number of broken bonds and the number of initial bonds. The yellow particles in Fig. 17 have zero damage, *i.e.* zero broken bonds. In contrast, blue particles have a damage value of 1, *i.e.* all bonds to adjacent particles are broken. Therefore,

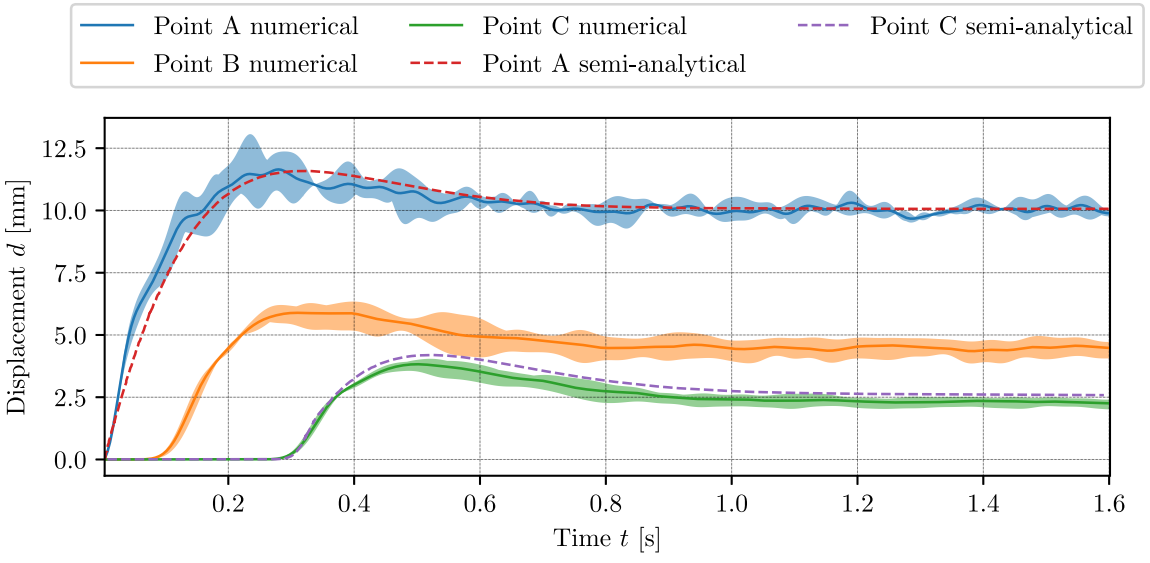

(a)

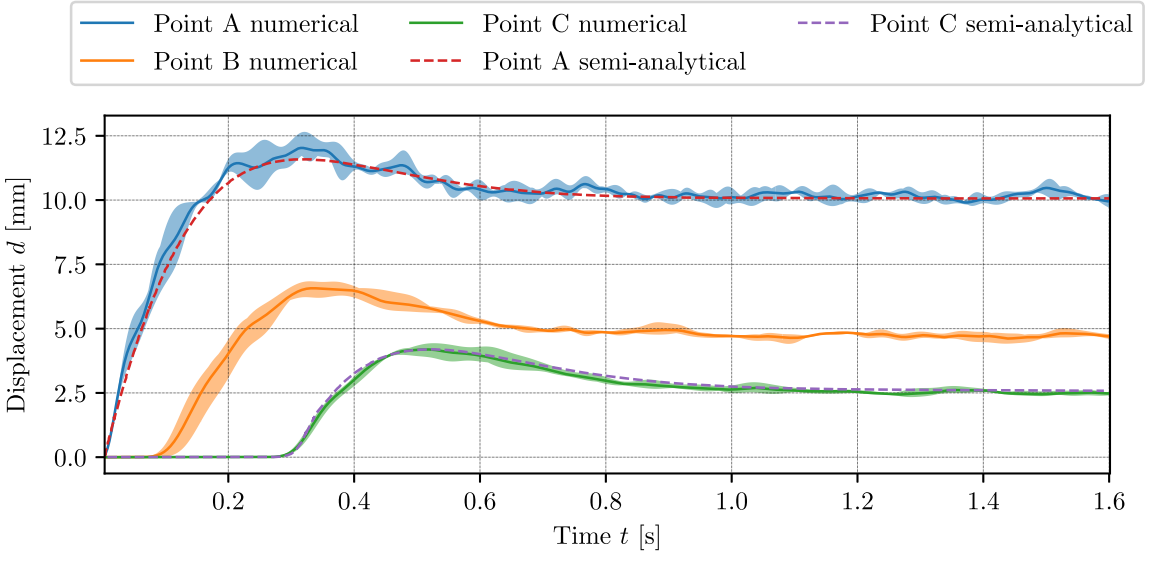

(b)

Fig. 11. Analytical and numerical displacement at cavity using: (a) particle size $D_{\text{ref}} = 25\,\text{cm}$ and (b) particle size $D_{\text{ref}} = 20\,\text{cm}$. (For interpretation of the references to colour in this figure legend, the reader is referred to the web version of this article.)

Fig. 17 allows for the analysis of crack propagation within the DEM region. It is noted that some cracks approach the interface but they do not interact with the BEM region.

5. Conclusions

This paper presents a novel interface DEM-BEM coupling approach in the time domain. The DEM is used to capture physical and geometrical non-linearities in the near field, whereas the BEM is used in the far field where linear elastic behaviour can be assumed. The proposed methodology circumvents incompatibilities between the methods to enable coupling. Virtual displacements transform the BEM tractions into equivalent nodal loads, which

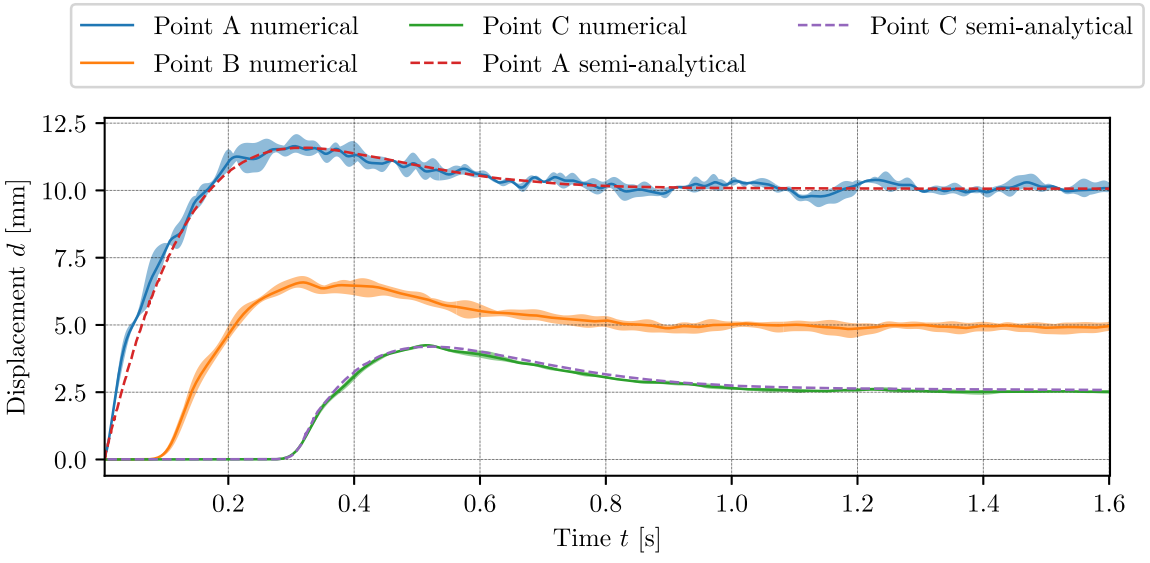

(a)

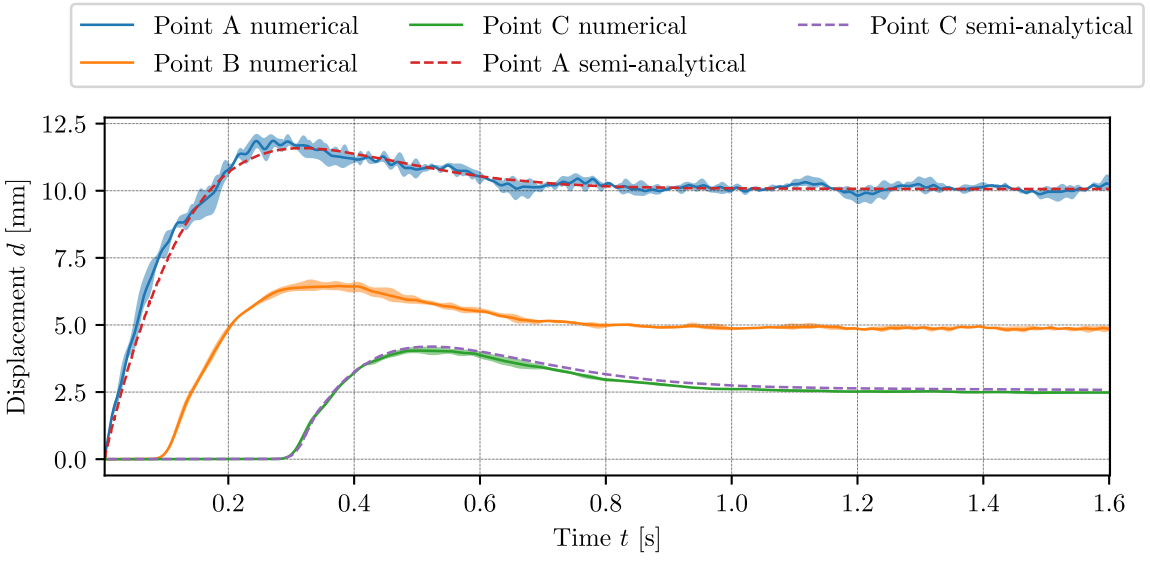

(b)

Fig. 12. Analytical and numerical displacement at cavity using: (a) particle size $D_{\text{ref}} = 15\,\text{cm}$ and (b) particle size $D_{\text{ref}} = 10\,\text{cm}$. (For interpretation of the references to colour in this figure legend, the reader is referred to the web version of this article.)

can be balanced with the point load of the particle. The DEM time integration scheme is reorganised to write an equation with the same terms as the BEM. Benchmark problems validate the methodology, and one application example evidences the great potential of the BEM-DEM coupling for computational geomechanics.

The first example shows excellent agreement between the results obtained with regular and irregular configurations of particle assemblies. This evidences that the coupling methodology can capture both normal and shear effects. In the second example, the semi-analytical and numerical results for internal displacements are in excellent agreement. This shows that the coupled method can accurately model wave propagation in the far field. Additionally, the results show that the effect of spurious waves is negligible. The last example introduces fracturing in the analysis.

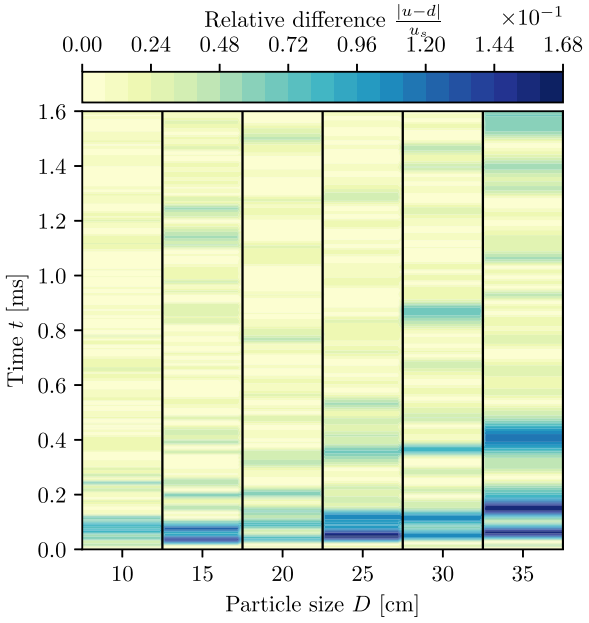

Fig. 13. Error in the displacement of point A normalised by static displacement.

The results show that the proposed BEM-DEM can represent combined fracturing and wave propagation phenomena in an infinite medium.

This paper is the first to successfully couple the BEM and DEM in the time domain for dynamic problems. The findings encourage using BEM-DEM to simulate real-life problems, which may require further study in future research. The simulations involved careful adjustment of the time step, with a smaller time step being beneficial for the DEM but leading to numerical instability for the BEM. To address this issue, a staggered scheme could provide greater flexibility in selecting different time steps for each method. The BEM also required a fine boundary discretisation due to the small particle size in the DEM, resulting in computational expenses for the BEM. However, compression schemes available in the literature and non-conforming discretisation may offer possible solutions to this challenge. The methodology presented here is general and can be extended to three-dimensional problems.

Declaration of competing interest

The authors declare the following financial interests/personal relationships which may be considered as potential competing interests: Klaus Thoeni and Jerzy Rojek reports financial support was provided by Australian Research Council.

Data availability

No data was used for the research described in the article

Acknowledgements

The authors would like to acknowledge the financial support of the Australian Research Council (DP190102407).

Appendix A. Supplementary data

Supplementary material related to this article can be found online at https://doi.org/10.1016/j.cma.2023.116040.

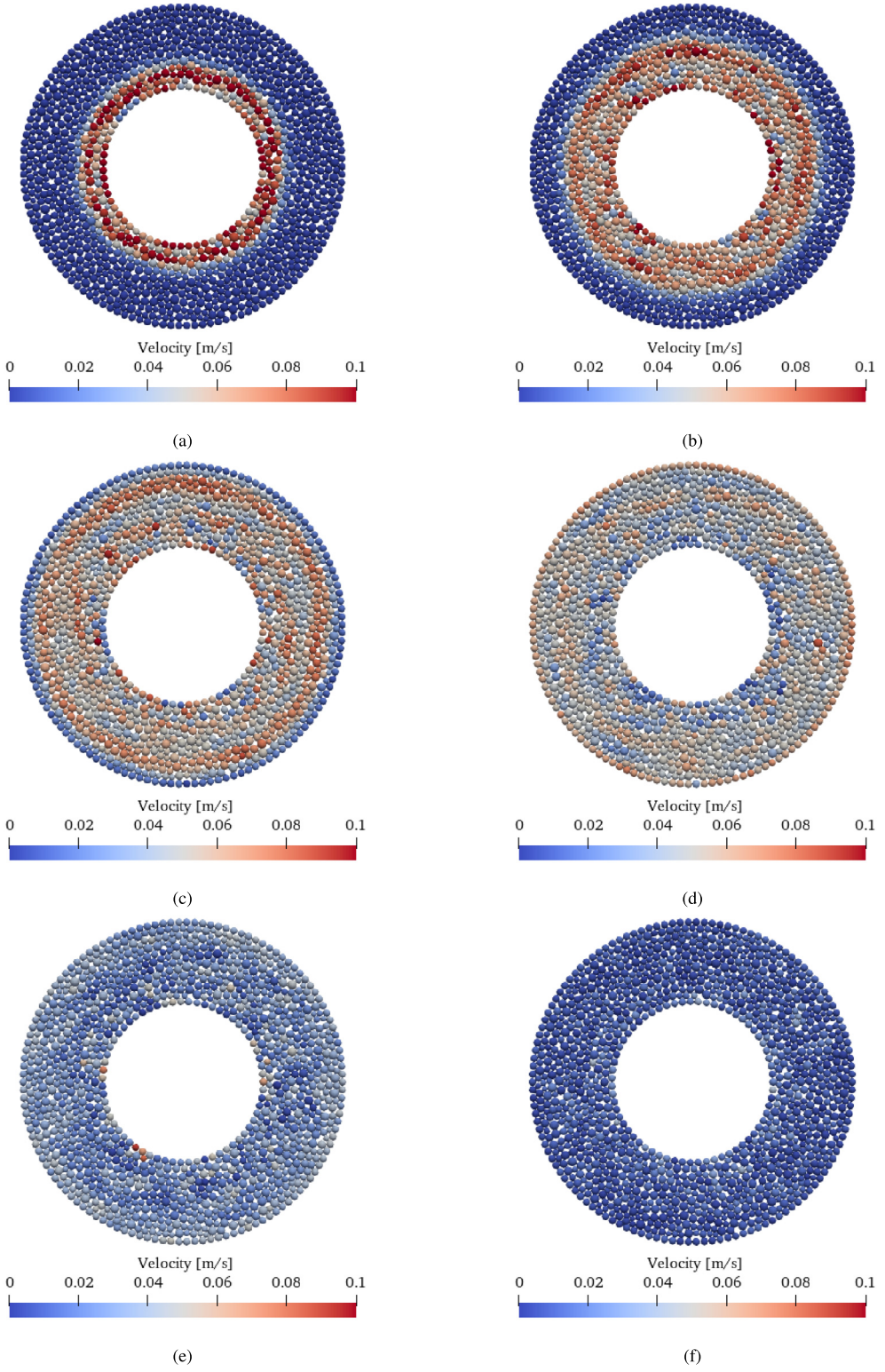

Fig. 14. Velocities at (a) 30 ms, (b) 60 ms, (c) 90 ms, (d) 120 ms, (e) 180 ms, and (f) 300 ms, using a particle assembly with reference particle size $D_{\text{ref}} = 10$ cm. See Appendix online version for the video.

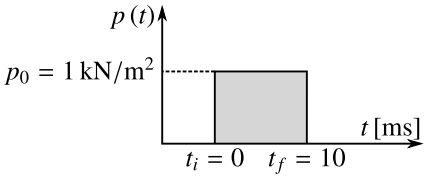

Fig. 15. Distribution of pressure over time.

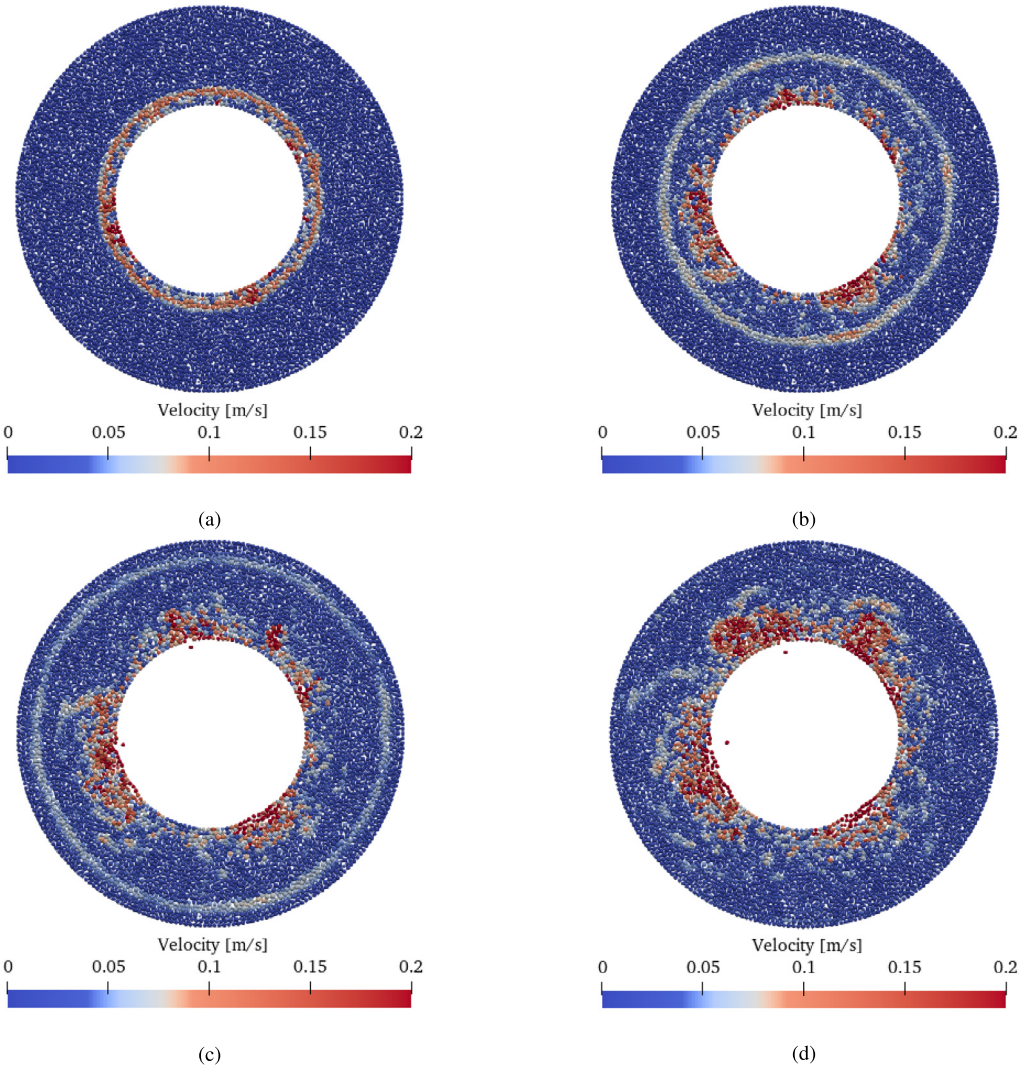

Fig. 16. Velocity at (a) 20 ms, (b) 60 ms, (c) 96 ms, and (d) 128 ms. See Appendix online version for the video.

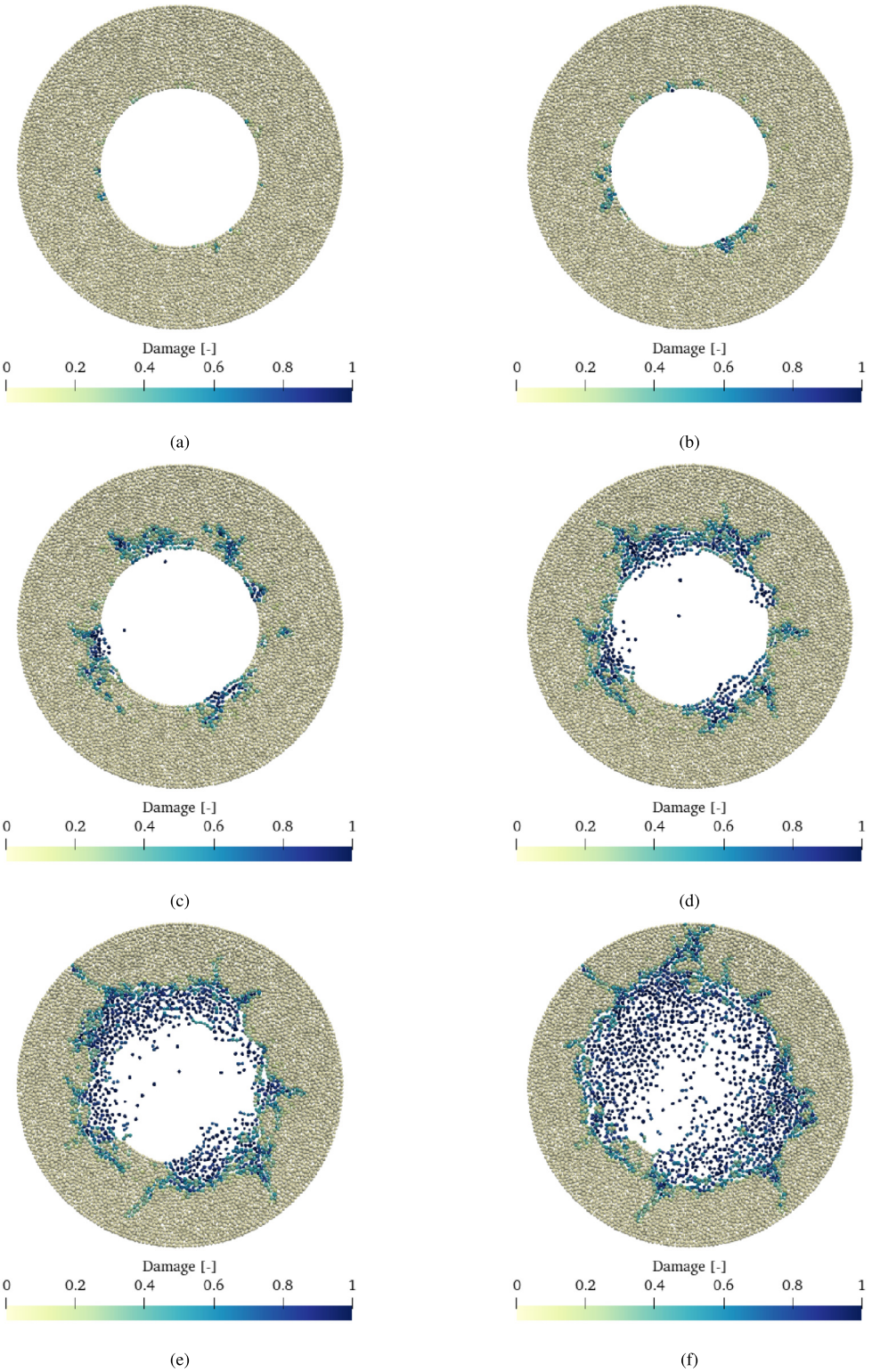

Fig. 17. Damage at (a) 20 ms, (b) 60 ms, (c) 160 ms, (d) 320 ms, (e) 600 ms, (f) 1.2 s. See Appendix online version for the video. (For interpretation of the references to colour in this figure legend, the reader is referred to the web version of this article.)

References

[1] F. Donzé, J. Bouchez, S. Magnier, Modeling fractures in rock blasting, Int. J. Rock Mech. Min. Sci. 34 (1997) 1153–1163.
[2] J. Yang, J. Sun, Y. Jia, Y. Yao, Energy generation and attenuation of blast-induced seismic waves under in situ stress conditions, Appl. Sci. 12 (2022) 9146.
[3] P. Baranowski, M. Kucewicz, M. Pytlik, J. Małachowski, Shock-induced fracture of dolomite rock in small-scale blast tests, J. Rock Mech. Geotechn. Eng. 14 (2022) 1823–1835.
[4] J.S. Vinod, DEM simulations in geotechnical earthquake engineering education, Int. J. Geotechn. Earthq. Eng. 1 (2010) 61–69.
[5] M. Panji, B. Ansari, Transient SH-wave scattering by the lined tunnels embedded in an elastic half-plane, Eng. Anal. Bound. Elem. 84 (2017) 220–230.
[6] T. Fras, P. Pawlowski, W. Li, T. Wierzbicki, Performance of Li-ion pouch battery under a high-velocity impact: experiment and numerical simulation, Int. J. Impact Eng. 155 (2021) 103915.
[7] Z. Wang, J. Yang, T. Zhang, C. Yao, X. Zhang, P. Gu, PPV and frequency characteristics of tunnel blast-induced vibrations on tunnel surfaces and tunnel entrance slope faces, Shock Vibr. 2021 (2021) 5527115.
[8] X. Feng, Q. Zhang, M. Ali, Explosion-induced stress wave propagation in interacting fault system: Numerical modeling and implications for chaoyang coal mine, Shock Vibr. 2019 (2019) 5856080.
[9] J. Carter, J. Booker, Sudden excavation of a long circular tunnel in elastic ground, Int. J. Rock Mech. Min. Sci. Geomech. Abstr. 27 (1990) 129–132.
[10] C. Labra, J. Rojek, E. Oñate, F. Zarate, Advances in discrete element modelling of underground excavations, Acta Geotechn. 3 (2008) 317–322.
[11] J. Rojek, E. Oñate, C. Labra, H. Kargl, Discrete element simulation of rock cutting, Int. J. Rock Mech. Min. Sci. 48 (2011) 996–1010.
[12] M. Jiang, Y. Dai, L. Cui, Z. Shen, X. Wang, Investigating mechanism of inclined CPT in granular ground using DEM, Granul. Matter 16 (2014) 785–796.
[13] D. Ambrosini, B. Luccioni, Effects of underground explosions on soil and structures, Undergr. Space 5 (2020) 324–338.
[14] J. Toraño, R. Rodríguez, I. Diego, J.M. Rivas, M.D. Casal, FEM models including randomness and its application to the blasting vibrations prediction, Comput. Geotechn. 33 (2006) 15–28.
[15] A.V. Krymskii, G.M. Lyakhov, Waves from an underground explosion, J. Appl. Mech. Techn. Phys. 25 (1984) 361–367.
[16] D. Michea, D. Komatitsch, Accelerating a three-dimensional finite-difference wave propagation code using GPU graphics cards, Geophys. J. Int. 182 (2010) 389–402.
[17] M. Bendezu, C. Romanel, D. Roehl, Finite element analysis of blast-induced fracture propagation in hard rocks, Comput. Struct. 182 (2017) 1–13.
[18] Z. You, W. Lord, Elastic wave propagation in an infinite media, in: D.O. Thompson, D.E. Chimenti (Eds.), Review of Progress in Quantitative Nondestructive Evaluation, Springer US, Boston, MA, 1990, pp. 133–140.
[19] Y. Heider, W. Markert, Dynamic wave propagation in infinite saturated porous media half spaces, Comput. Mech. 49 (2012) 319–336.
[20] G. Beer, J.O. Watson, Infinite boundary elements, Int. J. Numer. Methods Eng. 28 (1989) 1233–1247.
[21] W.J. Mansur, C.A. Brebbia, Formulation of the boundary element method for transient problems governed by the scalar wave equation, Appl. Math. Model. 6 (1982) 307–311.
[22] J. Dominguez, Boundary Elements in Dynamics, Elsevier Applied Science, London, 1993, p. 450.
[23] M. Schanz, Wave Propagation in Viscoelastic and Poroelastic Continua: A Boundary Element Approach, Springer-Verlag, Berlin, 2001.
[24] C.A. Brebbia, J.C.F. Telles, L.C. Wrobel, Boundary Elements Techniques, Springer-Verlag, Berlin Heidelberg, 1984.
[25] C. Duenser, G. Beer, Simulation of sequential excavation with the Boundary Element Method, Comput. Geotechn. 44 (2012) 157–166.
[26] S. Chaillat, M. Bonnet, J.F. Semblat, A new fast multi-domain BEM to model seismic wave propagation and amplification in 3-D geological structures, Geophys. J. Int. 177 (2009) 509–531.
[27] P.A. Cundall, O.D.L. Strack, A discrete numerical model for granular assemblies, Géotechnique 29 (1979) 47–65.
[28] D.O. Potyondy, P.A. Cundall, A bonded-particle model for rock, Int. J. Rock Mech. Min. Sci. 41 (2004) 1329–1364.
[29] B. Regassa, N. Xu, G. Mei, An equivalent discontinuous modeling method of jointed rock masses for DEM simulation of mining-induced rock movements, Int. J. Rock Mech. Min. Sci. 108 (2018) 1–14.
[30] A. Fakhimi, M. Lanari, DEM–SPH simulation of rock blasting, Comput. Geotechn. 55 (2014) 158–164.
[31] D. Song, X. Quan, M. Liu, C. Liu, W. Liu, X. Wang, D. Han, Investigation on the seismic wave propagation characteristics excited by explosion source in high-steep rock slope site using discrete element method, Sustainability 14 (2022) 17028.
[32] C. Labra, J. Rojek, E. Oñate, Discrete/finite element modelling of rock cutting with a TBM disc cutter, Rock Mech. Rock Eng. 50 (2017) 621–638.
[33] M. Lak, M. Fatehi Marji, A. Yarahmadi Bafghi, A. Abdollahipour, A coupled finite difference-boundary element method for modeling the propagation of explosion-induced radial cracks around a wellbore, J. Nat. Gas Sci. Eng. 64 (2019) 41–51.
[34] T. Zohdi, Computation of strongly coupled multifield interaction in particle–fluid systems, Comput. Methods Appl. Mech. Eng. 196 (2007) 3927–3950.
[35] R.E. Miller, E.B. Tadmor, A unified framework and performance benchmark of fourteen multiscale atomistic/continuum coupling methods, Model. Simul. Mater. Sci. Eng. 17 (2009) 053001.
[36] E. Oñate, J. Rojek, Combination of discrete element and finite element methods for dynamic analysis of geomechanics problems, Comput. Methods Appl. Mech. Eng. 193 (2004) 3087–3128.
[37] N.M. Azevedo, J.V. Lemos, Hybrid discrete element/finite element method for fracture analysis, Comput. Methods Appl. Mech. Eng. 195 (2006) 4579–4593.
[38] J. Rojek, E. Oñate, Multiscale analysis using a coupled discrete/finite element model, Inter. Multiscale Mech. 1 (2008) 1–31.

[39] S.P. Xiao, T. Belytschko, A bridging domain method for coupling continua with molecular dynamics, Comput. Methods Appl. Mech. Eng. 193 (2004) 1645–1669.
[40] P.T. Bauman, H.B. Dhia, N. Elkhodja, J.T. Oden, S. Prudhomme, On the application of the Arlequin method to the coupling of particle and continuum models, Comput. Mech. 42 (2008) 511–530.
[41] J. Rousseau, E. Frangin, P. Marin, L. Daudeville, Multidomain finite and discrete elements method for impact analysis of a concrete structure, Eng. Struct. 31 (2009) 2735–2743.
[42] X. Li, K. Wan, A bridging scale method for granular materials with discrete particle assembly - Cosserat continuum modeling, Comput. Geotechn. 38 (2011) 1052–1068.
[43] F. Zárate, E. Oñate, A simple FEM–DEM technique for fracture prediction in materials and structures, Comput. Part. Mech. 2 (2015) 301–314.
[44] F. Zárate, A. Cornejo, E. Oñate, A three-dimensional FEM–DEM technique for predicting the evolution of fracture in geomaterials and concrete, Comput. Part. Mech. 5 (2018) 411–420.
[45] A. Cornejo, V. Mataix, F. Zárate, E. Oñate, Combination of an adaptive remeshing technique with a coupled FEM–DEM approach for analysis of crack propagation problems, Comput. Part. Mech. 7 (2020) 735–752.
[46] O.C. Zienkiewicz, D.W. Kelly, P. Bettess, The coupling of the finite element method and boundary solution procedures, Int. J. Numer. Methods Eng. 11 (1977) 355–375.
[47] C. Brebbia, P. Georgiou, Combination of boundary and finite elements in elastostatics, Appl. Math. Model. 3 (1979) 212–220.
[48] G. Beer, Finite element, boundary element and coupled analysis of unbounded problems in elastostatics, Int. J. Numer. Methods Eng. 19 (1983) 567–580.
[49] O. von Estorff, M.J. Prabucki, Dynamic response in the time domain by coupled boundary and finite elements, Comput. Mech. 6 (1990) 35–46.
[50] G. Yu, W. Mansur, J. Carrer, S. Lie, A more stable scheme for BEM/FEM coupling applied to two-dimensional elastodynamics, Comput. Struct. 79 (2001) 811–823.
[51] D. Soares, W.J. Mansur, O.V. Estorff, An efficient time-domain FEM/BEM coupling approach based on FEM implicit Green's functions and truncation of BEM time convolution process, Comput. Methods Appl. Mech. Eng. 196 (2007) 1816–1826.
[52] D. Soares, W.J. Mansur, An efficient stabilized boundary element formulation for 2D time-domain acoustics and elastodynamics, Comput. Mech. 40 (2007) 355–365.
[53] D. Soares, W.J. Mansur, An efficient time-truncated boundary element formulation applied to the solution of the two-dimensional scalar wave equation, Eng. Anal. Bound. Elem. 33 (2009) 43–53.
[54] C. Lubich, Convolution quadrature and discretized operational calculus. I, Numer. Math. 52 (1988) 129–145.
[55] W. Moser, H. Antes, G. Beer, Soil-structure interaction and wave propagation problems in 2D by a Duhamel integral based approach and the convolution quadrature method, Comput. Mech. 36 (2005) 431–443.
[56] T. Rüberg, M. Schanz, Coupling finite and boundary element methods for static and dynamic elastic problems with non-conforming interfaces, Comput. Methods Appl. Mech. Eng. 198 (2008) 449–458.
[57] S. François, P. Coulier, G. Degrande, Finite element–boundary element coupling algorithms for transient elastodynamics, Eng. Anal. Bound. Elem. 55 (2015) 104–121.
[58] T. Burczynski, A. Mrozek, W. Kuś, A computational continuum-discrete model of materials, Bull. Pol. Acad. Sci. Techn. Sci. 55 (2007) 85–89.
[59] M. Mirzayee, N. Khaji, M. Ahmadi, A hybrid distinct element–boundary element approach for seismic analysis of cracked concrete gravity dam–reservoir systems, Soil Dyn. Earthq. Eng. 31 (2011) 1347–1356.
[60] L.J. Lorig, B.H.G. Brady, P.A. Cundall, Hybrid distinct element-boundary element analysis of jointed rock, Int. J. Rock Mech. Min. Sci. 23 (1986) 303–312.
[61] A.-B. Huang, M.Y. Ma, J.S. Lee, A micromechanical study of penetration tests in granular material, Mech. Mater. 16 (1993) 133–139.
[62] L. Malinowski, G.F. Karlis, G. Beer, J. Rojek, Iterative coupling of boundary and discrete element methods using an overlapping FEM zone, in: COUPLED IV: Proceedings of the IV International Conference on Computational Methods for Coupled Problems in Science and Engineering, CIMNE, 2011, pp. 301–312.
[63] G. Barros, A. Pereira, J. Rojek, K. Thoeni, DEM-BEM coupling in time domain for one-dimensional wave propagation, Eng. Anal. Bound. Elem. 135 (2022) 26–37.
[64] B. Chareyre, P. Villard, Dynamic spar elements and discrete element methods in two dimensions for the modeling of soil-inclusion problems, J. Eng. Mech. 131 (2005) 689–698.
[65] R. Hosn, L. Sibille, N. Benahmed, B. Chareyre, Discrete numerical modeling of loose soil with spherical particles and interparticle rolling friction, Granul. Matter 19 (2017) 1–12.
[66] V. Smilauer, V. Angelidakis, E. Catalano, R. Caulk, B. Chareyre, W. Chèvremont, S. Dorofeenko, J. Duriez, N. Dyck, J. Elias, B. Er, A. Eulitz, A. Gladky, N. Guo, C. Jakob, F. Kneib, J. Kozicki, D. Marzougui, R. Maurin, C. Modenese, G. Pekmezi, L. Scholtès, L. Sibille, J. Stransky, T. Sweijen, K. Thoeni, C. Yuan, Yade Documentation, The Yade Project, 2021, http://dx.doi.org/10.5281/zenodo.5705394.
[67] W.J. Mansur, J.A.M. Carrer, Two dimensional transient BEM analysis for the scalar wave equation: Kernels, Eng. Anal. Bound. Elem. 12 (1993) 283–288.
[68] H. Cheng, T. Shuku, K. Thoeni, P. Tempone, S. Luding, V. Magnanimo, An iterative Bayesian filtering framework for fast and automated calibration of DEM models, Comput. Methods Appl. Mech. Eng. 350 (2019) 268–294.
[69] P. Hartmann, H. Cheng, K. Thoeni, Performance study of iterative Bayesian filtering to develop an efficient calibration framework for DEM, Comput. Geotechn. 141 (2022) 104491.